High-Field Nuclear Magnetic Resonance (NMR) Spectroscopy

34

Nicholas Jaegers, Nancy M. Washton, Yong Wang, and Jian Zhi Hu

Contents

Abstract

Nuclear magnetic resonance (NMR) is a nondestructive spectroscopic technique that provides detailed molecular structural information via the electronic environments of nuclei in materials. Enhanced magnetic field strengths offer potential increases to the resolution of the NMR measurement, enabling discernment of unique chemical environments that might not be possible at low fields. Herein, the application of high-field NMR to catalyst and electrochemical system characterization is detailed. A brief description of NMR and quadrupolar nuclei is presented where the effects of magnetic field are described. Examples of high-field NMR are provided with particular focus on employing NMR to elucidate the structure of oxides of aluminum and vanadium for catalyst applications. The role of high-field NMR to conduct challenging experiments for energy storage materials is also explored, and numerous other nuclei which require high-field measurement are briefly summarized.

Keywords

Catalyst · Spectroscopy · NMR · High-field · Quadrupolar · ^{27}Al · ^{51}V · Metal oxide

34.1 A Brief Introduction of NMR for Catalyst Characterization

The industrial significance of catalysts stimulates unwavering efforts to detail the underlying material structures and characteristics [1]. Such efforts have relied upon numerous catalyst characterization methods to probe their structures and reactive properties. Spectroscopic techniques are of great importance due to the diverse array of information they can provide, be it detection of active surface structures, reaction intermediates, or interactions between substrates and catalysts. Nuclear magnetic resonance (NMR) is a particularly powerful technique for the nondestructive analysis of chemical species. NMR is capable of probing the detailed three-dimensional molecular structures in a quantitative fashion and molecular dynamics through electronic environment of nuclei upon exposure to a strong magnetic field. The NMR signal arises from detected electromagnetic radiation that is emitted from the nucleus of an atom. The frequency of such emissions typically spans from 10 MHz to 1 GHz or more, which are stimulated by the excitation of these nuclei. Without the application of an external magnetic field, the spin states of the nuclei are oriented randomly and energetically degenerate. However, exposure to a magnetic field causes spin states to preferentially orient themselves such that the

N. Jaegers · Y. Wang · J. Z. Hu (✉)
Physical and Computational Science Directorate, Pacific Northwest National Laboratory, Richland, WA, USA

The Gene and Linda Voiland School of Chemical Engineering and Bioengineering, Washington State University, Pullman, WA, USA
e-mail: Nicholas.jaegers@pnnl.gov; yong.wang@pnnl.gov; jianzhi.hu@pnnl.gov

N. M. Washton
Physical and Computational Science Directorate, Pacific Northwest National Laboratory, Richland, WA, USA
e-mail: Nancy.washton@pnnl.gov

I. E. Wachs, M. A. Bañares (eds.), *Springer Handbook of Advanced Catalyst Characterization*, Springer Handbooks,
https://doi.org/10.1007/978-3-031-07125-6_34

induced magnetic field of the nuclear spin aligns with the external field. This generates a separation in the energy levels of those spin states in alignment and those opposing the external field, a phenomenon called the Zeeman effect (Fig. 34.1 for spin $I = 1/2$). Spins of high energy oppose the external magnetic field and are present in populations that are controlled by thermodynamic equilibrium. A Boltzmann distribution (Eq. 34.1) describes the population of the spin states, where N represents the number of the spins in either the upper and lower energy levels (U or E, respectively), ΔE is the energy difference between the two states, T represents the temperature, and k is the Boltzmann constant:

$$\frac{N_u}{N_l} = e^{-\Delta E/kT} \tag{34.1}$$

Nuclear spins are sometimes described as possessing angular frequency of precession around the applied magnetic field (ω) [2]. This angular rate of recurrence is termed the Larmor frequency and is characteristic of the nucleus through the gyromagnetic ratio (γ) and directly proportional to the applied field strength (B_0) as related by Eq. 34.2. The Larmor frequency also directs the Zeeman Energy, shown by Eq. 34.3:

$$\omega^0 = \gamma B^0 \tag{34.2}$$

$$\omega = 2\pi v = \frac{\Delta E}{2\pi h} \tag{34.3}$$

By applying a radio-frequency pulse near the energy of Zeeman splitting, spins in the low-energy state can be excited to the high-energy state, in the process generating a precessing transverse magnetization. Rotation of the magnetic movement from the transverse magnetization induces a voltage inside the detection coil of the NMR probe which generates a rotating magnetic field that, in turn, generates an electric field. The electric field interacts with the electrons present within the NMR detection coil, and the interaction is recorded as the free induction decay (FID), the precursor to the NMR spectra which is arrived at through Fourier transformation. The local electronic structure around the nucleus of a given chemical species determines the energy of the spin precession and is responsible for the unique chemical shifts observed for different species that enable the detection of an array of signals in the spectrum. Such a spectroscopic method is inherently insensitive, arising from the minute excess of the low-energy spin population over the high-energy spins due to the achievable magnetic field strength and often low natural abundance of the nuclei, necessitating repeated scans of the same sample for improved signal distinction exceeding noise levels which arise from the thermal motion of electrons present within the receiver coil.

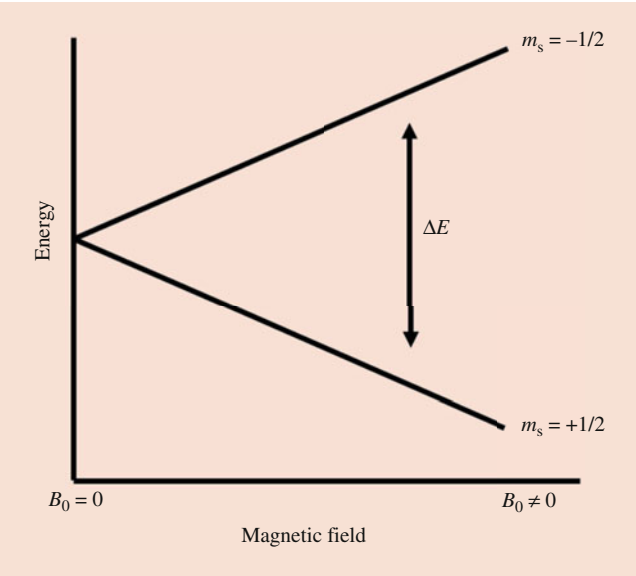

Fig. 34.1 Representation of the Zeeman effect for nuclear spins

Any nucleus with spin ($I \neq 0$) will exhibit such properties in a magnetic field. This criterion qualifies a cornucopia of nuclei for detection by NMR, enabling the observation of the chemical environments of both catalyst materials, probe molecules, and reactive substrates. A selection of such nuclei includes ^{1}H, ^{2}H, ^{6}Li, ^{7}Li, ^{11}B, ^{13}C, ^{14}N, ^{15}N, ^{17}O, ^{19}F, ^{23}Na, ^{25}Mg ^{27}Al, ^{29}Si, ^{31}P, ^{33}S, ^{35}Cl, ^{37}Cl ^{47}Ti, ^{49}Ti, ^{51}V, ^{67}Zn, ^{91}Zr, ^{95}Mo, ^{97}Mo, ^{133}Cs, ^{139}La, ^{183}W, ^{207}Pb, and numerous others. The quantitative examination of such a wide selection of nuclei garners strong advantages which can be exploited to supplement alternative spectroscopic techniques. Though expansive, not all nuclei with spin are practical to observe with NMR. Sensitivity is a notable challenge for NMR, where repeated scans help to enhance the signal-to-noise ratio, but this improves by the square root of the number of scans ($S/N \propto \text{scans}^{0.5}$). For dilute species, it is clear that the resolution necessary may too resource-intensive for practical observation. To overcome this challenge, isotope enrichment is frequently employed to boost the signal since $S/N \propto$ spins. For example, isotopic enrichment of a ^{13}C species can improve the signal by nearly 100-fold over natural abundance, which saves a factor of 10,000 in the number of scans (~ day of data acquisition). Another factor that contributes to the sensitivity is the gyromagnetic ratio of the nucleus. The intrinsic sensitivity of a nucleus is proportional to γ^3. Beyond this, how broad the spectral features are can further limit the observation of nuclei. Another way to enhance the sensitivity of the NMR signal is to employ a stronger magnet, which had a direct relationship to the number of spins available for excitation (Eq. 34.1).

Special techniques are required to analyze solid samples with high spectral resolution, a popular choice being a

technique known as magic angle spinning (MAS) [3, 4]. The MAS technique addresses the orientation-dependent (anisotropic) interactions of NMR by rotating a given sample at the magic angle – 54.7356° with respect to the magnetic field – drastically narrowing the lines observed in solids and introducing a spinning sideband manifold to the spectra from spin echos [5]. The line narrowing is realized due to the form of the Hamiltonian which accounts for the energetic interactions between the nuclear spin and magnetic field. Further details are available elsewhere, but MAS NMR is widely regarded as an essential tool to conduct advanced characterization on solid catalyst samples [6, 7].

NMR provides a wealth of information about chemical systems that might otherwise be challenging to obtain. On a foundational level, the spectroscopic technique provides a measure of the electronic shielding around the nucleus of an atom. This shielding is modulated by the structure, coordination, electric charge, and outer shell interactions (first, second, third, etc.). These differences in electronic environment give rise to the contrasting chemical shifts, which make species distinction by NMR possible. Given that such environments are typically non-static, it is appropriate to note that NMR provides the average configuration over the time span of signal accumulation (~10 ms). If desired, however, extraction of such dynamic behaviors as rotation, translation, and reactivity is achievable [8]. For example, the peak width can often be related to the uniformity or mobility of a given sample, and multiple pulse sequences can provide information about the length of time spins interact (tumbling rate). Further, the interchange between two species, chemical exchange, is also an observable phenomenon with measurable rates [9]. Employing multitude of pulse sequences available dramatically extends the information accumulated from an NMR experiment. Cross polarization is a common pulse sequence used to achieve this goal. In this method, abundant spin species (often ^{1}H) are excited by an rf pulse, and the resulting magnetization is transferred to a less abundant species to enhance the signal of less abundant nuclei which are located nearby and relatively immobile.

A more complex class of experiment can provide powerful information regarding the structure and coordination of nuclei in a catalyst system. Two-dimensional experiments comprise those whereby a series of free induction decay profiles are collected with a modulated time-dependent variable. Several popular homonuclear correlation experiments exist which establish the interactions between species in chemical substrates. For example, COrrelated SpectrscopY (COSY), TOtal Correlation SpectroscopY (TOCSY), Incredible Natural Abundance DoublE-QUAntum Transfer Experiment (INADEQUATE), and Adequate DoublE-QUAntum Transfer Experiment (ADEQUATE) all take advantage of spin-spin coupling to demonstrate species which are connected through direct bonds. More advanced pulse sequences to directly characterize the catalyst, however, can provide unique insight into the structure of the materials. Frydman introduced the multiple-quantum magic angle spinning (MQMAS) experiment for half-integer quadrupole spins which greatly enhances the resolution of the sample's NMR spectra [10, 11]. As will be detailed below, quadrupolar nuclei can be challenging to characterize, but MQMAS takes advantage of nonconsecutive energy transitions to provide a detailed view of the nuclear spin system and reveal chemically inequivalent sites which would otherwise be convoluted. Representative applications of MQMAS will be highlighted in later sections.

In addition to extracting information from a variety of pulse sequences, the employment of probe molecules and in situ NMR has dramatically expanded the possible descriptions of catalyst systems. For example, acid-base properties have been assessed by the introduction of probe molecules to the material [12, 13]. Recently, in situ solid-state NMR techniques have been developed which enable the observation of catalysts and substrates under controlled conditions including elevated temperatures and pressures [14–16]. Such technology has enabled a detailed understanding of the active centers of catalysts as well as how these sites are modulated under environmental influence [17, 18]. While such in situ MAS NMR contributes much the understanding of catalytic systems, this chapter considers the contributions of high-field NMR on the study of quadrupolar nuclei, including the ongoing development of high-field, high-temperature, high-pressure MAS NMR. The effects of quadrupolar nuclei will be outlined alongside a description of high-field NMR. Subsequently, applications of high-field NMR to better understand catalyst stems will be provided with an emphasis on ^{27}Al and ^{51}V MAS NMR.

34.2 High-Field NMR and Quadrupolar Nuclei

The strength of a magnetic field has a dramatic impact on NMR spectroscopy. As described by Eqs. 34.1–34.3, higher fields contribute to a larger energetic separation between the low- and high-energy spin states in a nucleus. This results in a larger population difference which enables a greater quantity of spins be excited and detected during experimentation. This directly results in enhanced resolution and sensitivity for a given sample in the same sample volume. This is directly advantageous for nuclei with poor overall sensitivity. It is also beneficial for isotopes which do not possess a uniform electric field around the nucleus. Nuclei with spin exceeding one-half possess a nonspherical electric charge distribution, which gives rise to the nuclear quadrupole interaction. Unlike spin 1/2 nuclei, asymmetries in the charge distribution surrounding the nuclei interact with the electric field gradient and generates $(2I + 1)$ energy levels when exposed to an

external magnetic field. For example, a spin 3/2 nucleus would exhibit four energy levels as shown in Fig. 34.2 instead of just two for spin 1/2 as shown in Fig. 34.1. These energy levels can be further perturbed by first- and second-order quadrupolar interactions [19–25].

The quadrupolar interaction also can cause fluctuations in electric field gradient that often manifest as shorter relaxation of the nuclear spins and consequently decrease the signal intensity and broaden the NMR signature. This notably challenges the spectral acquisition of quadrupolar nuclei and hinders characterization of a wide range of materials. Since each nuclear environment will experience different asymmetry in the gradient, the properties which describe the quadrupolar nature of the species can be a useful characterization tool. For example, the asymmetry parameter, η_Q, is a measure of anisotropy in the lineshape and can be derived from the electrostatic potential of the electric field gradient in a given direction, $V(r)$ (Eq. 34.4). This property can be determined by fitting either a spinning sideband manifold or a wide-line powder NMR pattern. Further, the quadrupole moment, eQ, can be described as prolate (>0) or oblate (<0) and is a component of the electric field gradient Q tensor and quadrupole coupling constant, C_Q, described by Eq. 34.5:

$$\eta_Q = \frac{V_{XX} - V_{YY}}{V_{ZZ}} \tag{34.4}$$

$$X_Q = C_Q = \frac{eQ}{h} V_{ZZ} = \frac{e^2 qQ}{h} \tag{34.5}$$

First- and second-order perturbations which arise from the quadrupolar interactions can be applied to the spin state energy difference to directly calculate the transition energies. In the limit of high magnetic field strength, the quadrupole interaction alters the Zeeman states in the laboratory frame. Equations 34.6 and 34.7 quantify this energy where θ and φ are the Euler angles, m is the magnetic quantum number associated with the Zeeman levels, I is the nuclear spin, η is the asymmetry parameter, h is Planck's constant, X_Q is the quadrupole coupling constant, e is the fundamental charge, Q is the nuclear quadrupole moment, and q is the greatest component of the electric field gradient q-tensor [26, 27]. When added to the Zeeman energy, modulated first- and second-order quadrupolar energies ($E^{(1)}$ and $E^{(2)}$) give the energy of each level. The transition energy can be calculated by noting the difference in energy between a given pair of levels. Such differences for consecutive levels are directly shown in Figs. 34.2, 34.3, 34.4, and 34.5, where the visual magnitude is approximated. Care should be taken when selecting the source for these equations [28, 29]:

$$E^{(1)} = \frac{X_Q h}{8I(2I-1)} \left[3\cos^2\theta - 1 + \eta \sin^2\theta \cos 2\varphi\right] \times \left(3m^2 - I(I+1)\right) \tag{34.6}$$

$$E^{(2)} = -\left(\frac{e^2 qQ}{4I(2I-1)}\right)^2 \frac{m}{\nu_0} \left[-\frac{1}{5}\left(I(I+1) - 3m^2\right)\left(3+\eta^2\right) + \frac{1}{28}\left(8I(I+1) - 12m^2 - 3\right)\left(\left(\eta^2 - 3\right)\left(3\cos^2\theta - 1\right) + 6\eta^2 \sin^2\theta \cos 2\varphi\right) + \frac{1}{8}\left(18I(I+1) - 34m^2 - 5\right) \times \left(\frac{1}{140}\left(18+\eta^2\right)\left(35\cos^4\theta - 30\cos^2\theta + 3\right) + \frac{3}{7}\eta \sin^2\theta\left(7\cos^2\theta - 1\right)\cos^2\varphi + \frac{1}{4}\eta^2 \sin^4\theta \cos 4\varphi\right)\right] \tag{34.7}$$

When conditions of axial symmetry ($\eta = 0$) are valid, the energy pre-factor for the first-order terms as a function of nuclear spin and magnetic quantum number is provided for

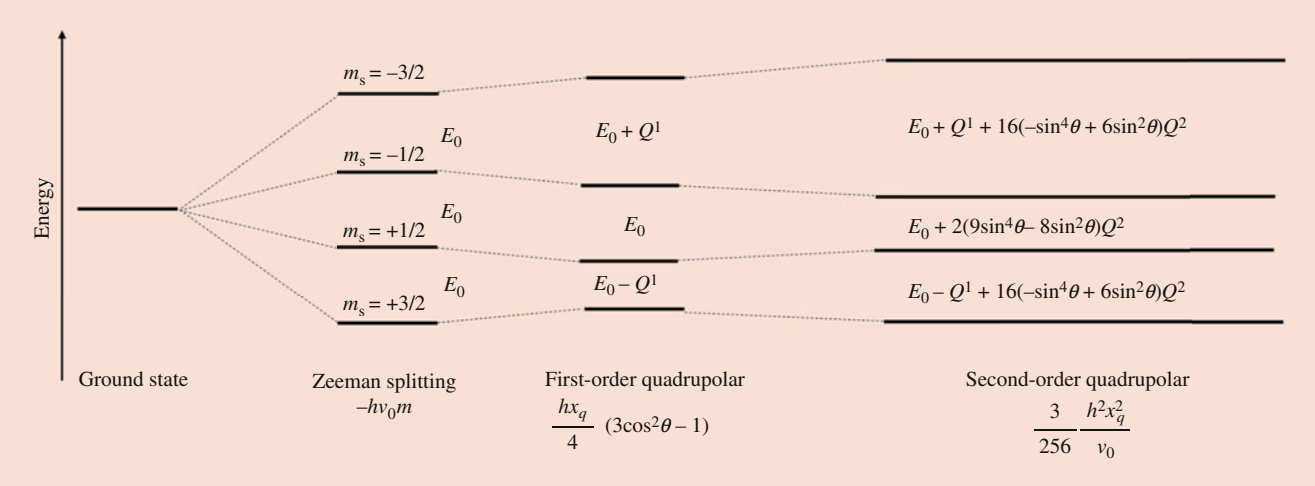

Fig. 34.2 Energy-level diagram for a spin 3/2 nucleus listing the energy level difference for each spin state as first- and second-order quadrupolar terms are applied

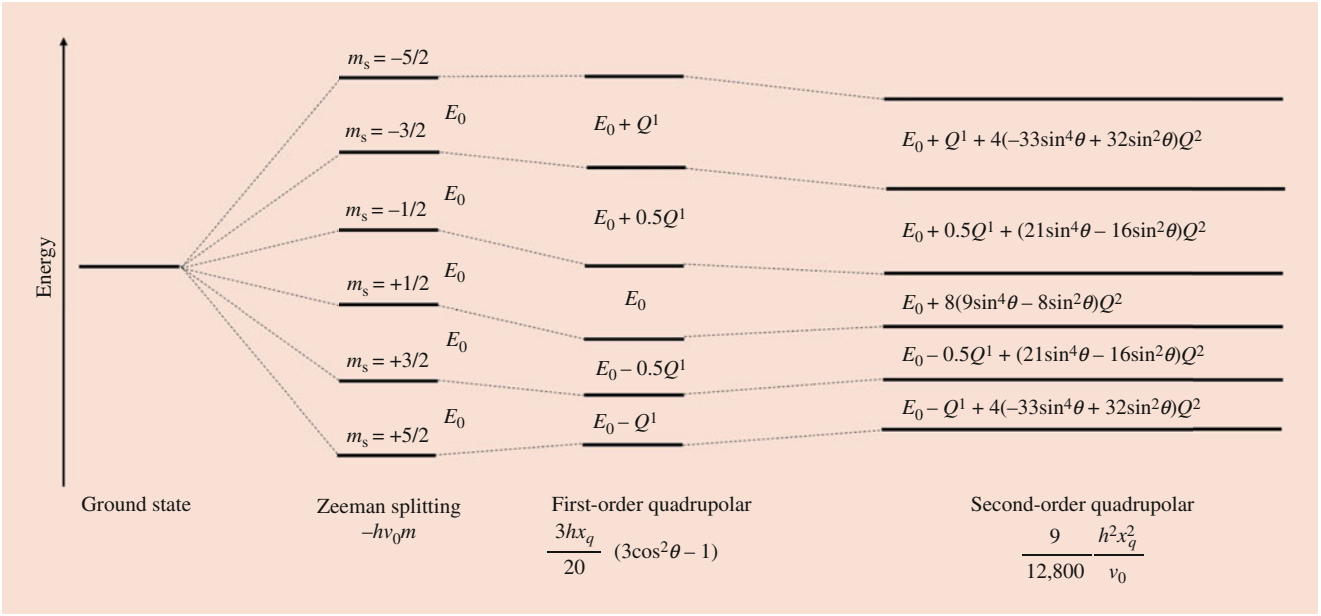

Fig. 34.3 Energy-level diagram for a spin 5/2 nucleus listing the energy level difference for each spin state as first- and second-order quadrupolar terms are applied

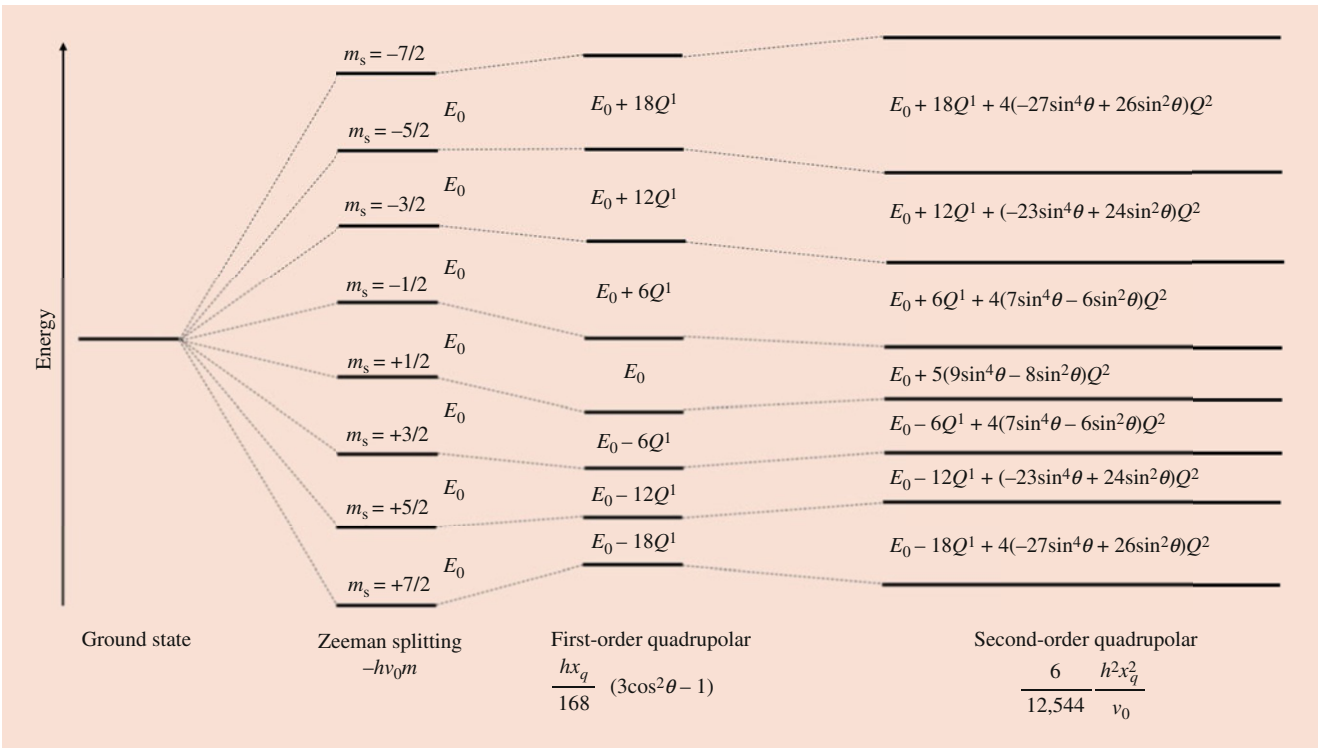

Fig. 34.4 Energy-level diagram for a spin 7/2 nucleus listing the energy level difference for each spin state as first- and second-order quadrupolar terms are applied

several quadrupolar half-integer spins in Table 34.1. Again, the transition energy can be derived from the difference between these two energy states (depicted in Figs. 34.2, 34.3, 34.4, and 34.5 for spin three-, five-, seven-, and nine-half nuclei). It is shown that the $-1/2$ and $1/2$ first-order quadrupolar energy perturbation terms are the same for all

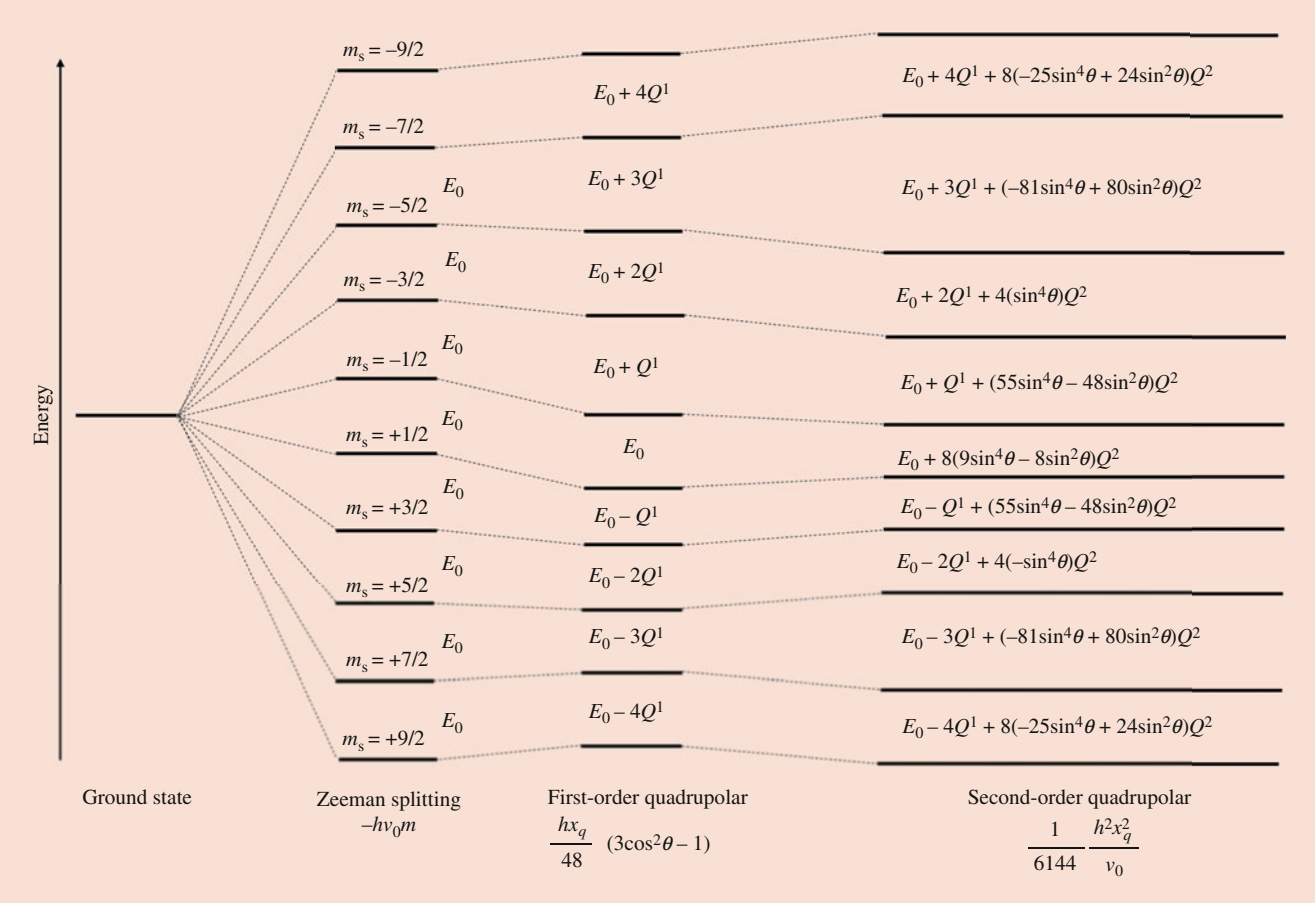

Fig. 34.5 Energy-level diagram for a spin 9/2 nucleus listing the energy level difference for each spin state as first- and second-order quadrupolar terms are applied

Table 34.1 First-order quadrupolar energy perturbation coefficients for quadrupolar half-integer spins

$m\backslash I$	3/2	5/2	7/2	9/2
−9/2				1/8
−7/2			1/8	1/24
−5/2		1/8	1/56	−1/48
−3/2	1/8	−1/40	−3/56	−1/16
−1/2	−1/8	−1/10	−5/56	−1/12
1/2	−1/8	−1/10	−5/56	−1/12
3/2	1/8	−1/40	−3/56	−1/16
5/2		1/8	1/56	−1/48
7/2			1/8	1/24
9/2				1/8

The energy is the product of the coefficient and $hXq^*(3\cos 2\theta - 1)$

half-integer spins, demonstrating that the central transition energy is unaffected by first-order effects. It is shown in the equation and expressed in the energy diagrams that the magnitude of $E^{(1)}$ depends not on the strength of the external magnetic field, but it is proportional to the quadrupole coupling constant. By assessing the governing equation, it can be seen that first-order quadrupolar perturbations can be eliminated under the condition of magic angle spinning at sample spinning rates far greater than the width of the first-order quadrupolar interaction (infinite spinning rate). This arises from the $3\cos^2\theta - 1$ term for which coefficients are provided in Table 34.1. When infinite MAS is satisfied, this term approaches zero. Eq. 34.7 shows that the second-order perturbations have a less straightforward relationship with the orientation (θ), spin number (I), and Zeeman level (m). The square dependence on m for first-order corrections shifts in the same direction for $+m$ and $-m$; however, this is not the case for second-order corrections. These second-order coefficients in the limit of MAS are provided in Table 34.2. Even under such conditions, second-order contributions are retained. Unlike for first-order effects, the central transition is altered since the energy shifts for $+m$ and $-m$ are opposite in magnitude due to a dependence on both m and m^3. Further disparities from the first-order correction are revealed when considering that first-order terms increase with X_Q and the second-order terms increase with ${X_Q}^2$. The second-order correction also contains an orientation-independent term, showing that the isotropic chemical shift has contributions from quadrupole coupling. Notably, the second-order quadrupolar perturbation is inversely proportional to the

Table 34.2 Second-order quadrupolar energy perturbation coefficients for quadrupolar half-integer spins under MAS

$m\backslash I$	3/2	5/2	7/2	9/2
−9/2				17/2304
−7/2			13/1344	7/6912
−5/2		9/640	−5/9408	−25/13824
−3/2	5/192	−3/640	−31/9408	−29/13824
−1/2	−1/64	−3/800	−5/3136	−1/1152
1/2	1/64	3/800	5/3136	1/1152
3/2	−5/192	3/640	31/9408	29/13824
5/2		−9/640	5/9408	25/13824
7/2			−13/1344	−7/6912
9/2				−17/2304

The energy is the product of the coefficient and $(hX_q)^2$

frequency and thus field strength. For this reason, high-field magnets provide advantages when conducting NMR experiments on quadrupolar nuclei. If axial symmetry is achieved, second-order energy perturbations can be simplified.

Contrasting X_Q and η between species in a given sample can give rise to unintended selective excitation of a particular spin species. For example, large X_Q will exaggerate the separation between adjacent levels and promote contrasting pulse responses that render quantification challenging. This issue is typically alleviated by employing very small pulse lengths to reduce the tip angle and render selective excitation to be effectively absent. In addition to describing the nature of the nuclear spin, the quadrupolar parameters can be used to simulate the lineshape of spin-half nuclei. Second-order quadrupolar effects are decreased at sufficiently high magnetic fields under MAS conditions, since quadrupolar broadening is inversely proportional to magnetic field strength (Eq. 34.7) [30]. Under such conditions, the spectral resolution may be improved, and the resulting lines may be suitably symmetric to fit with a simple Gaussian/Lorentzian simulated lineshape. Though first-order quadrupolar effects can be eliminated by spinning at the magic angle, second-order effects remain since the angle required to eliminate them is dissimilar to the magic angle, resulting in only partially averaged second-order quadrupolar effects [31]. When the rotation rate of the sample is lower than the frequency domain width of the static sample spectrum, spinning sidebands appear for which the overall SSB profile resembles the general shape of the static powder pattern. The static powder pattern is a projection of the NMR spectrum of all orientations of single-crystal transitions [32]:

$$\Delta\nu \propto \frac{1}{\gamma B_0} \tag{34.8}$$

In addition to suppressing these quadrupolar effects, magnetic field strength has an impact on the resolution on the acquired spectra. The linewidth is inversely proportional to both the gyromagnetic ratio and the magnetic field, so at high-field strengths, greater sensitivity can be achieved (Eq. 34.8). A prototypical example can be found in an investigation of hexamethylborazine [33]. Under conditions of magic angle spinning, the NMR spectrum is both incompletely narrowed and shifted from the true isotropic position due to quadrupolar contributions. This contribution decreases with increasing field strength, which shifts the line closer to the isotropic position and narrows the feature to provide enhanced resolution.

As a brief way to visualize how such quadrupolar interactions impact the spectrum, Fig. 34.6 displays simulations of the lineshapes for second-order quadrupolar interactions (which cannot be removed by MAS) with different asymmetry parameters (η) and magnetic field strengths of 9, 14, 20, and 40 T. At higher fields, this effect is suppressed, narrowing the observed linewidth. Also shown is the impact that the field strength has on the chemical shift anisotropy. This increases with field strength, leading to undesired broadening (in hertz), though typically retains comparable linewidth in the ppm domain since it is proportional to the external field strength. Both the broad static line and set of spinning sidebands are shown for the chemical shift anisotropy. Indeed, the quarupolar lineshape adds complexity and broadens the spectrum and when combined with other NMR effects can induce highly irregular spectral patterns. These are just a sample of how these interactions effect the NMR lineshape. Dipolar coupling, Knight shift, and others may also impact the observed spectrum. An extended account of how various interactions can impact the NMR spectra can be found in *eMagRes* [19]. The lineshapes presented herein were simulated using dmfit, a software packed that simulates and fits spectra with numerous models to account for different NMF interactions [20]. Fitting and quantification are topics of interest on its own [21]. There are a number of software packages that can be used to simulate quadrupolar spectra: QuadFit [22], VnmrJ [23], ssNake [24], and QUEST [25] are representative of a body of software available.

Such changes to the spectral resolution of quadrupolar nuclei have been directly measured using solid-state ^{27}Al MAS NMR [34, 35]. As shown in Fig. 34.7, for two samples of zeolite framework BEA, the magnetic field for a given sample can be modulated (7, 12, 20 T), and the resulting spectra can be compared. The low-field spectra reveal broad lines near 60 ppm ascribed to tetrahedral aluminum species that heavily overlap and are not resolved. At higher magnetic fields, the lines narrow, and a clear shoulder is present on the low-field side of the spectrum. At even greater field strengths, the lines are resolved from each other. In contrast, the narrow features near 0 ppm ascribed to extra-framework aluminum are relatively unaffected by field strength. The results indicate

that the tetrahedral aluminum species suffer from broadening induced by second-order quadrupolar interactions. These interactions are inversely proportional to the field strength and greatly suppressed at 20 T. Observations made at high field enable the observation of unique aluminum tetrahedral species where such a distinction is not possible at low-field strengths where overlapping of the signals results in a somewhat ambiguous assignment.

Such observations become increasingly apparent at even high-field strengths. Recently, Bruker has revealed an ultra-high-field 1.2 GHz NMR (28.2 T), which represents a dramatic enhancement over previous technologies [36]. While

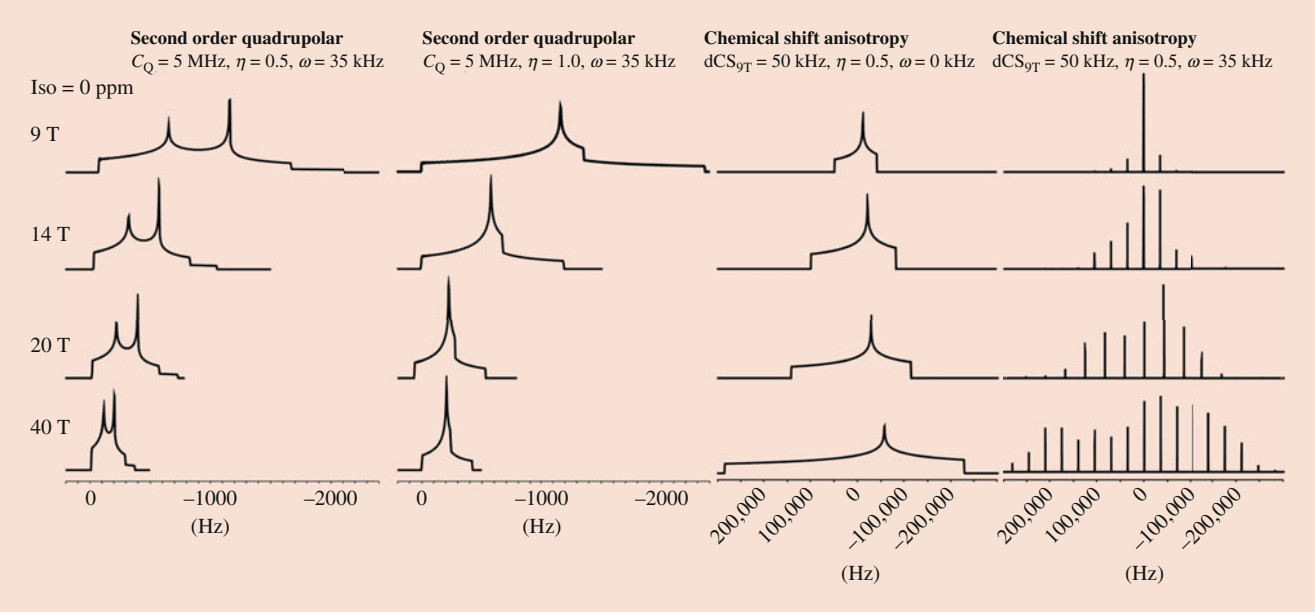

Fig. 34.6 Simulated ^{51}V NMR spectra for species which exhibit second-order quadrupolar and chemical shift anisotropy-induced lineshapes with the parameters specified at several external magnetic field strengths. All species were simulated with an isotropic chemical shift of 0 ppm

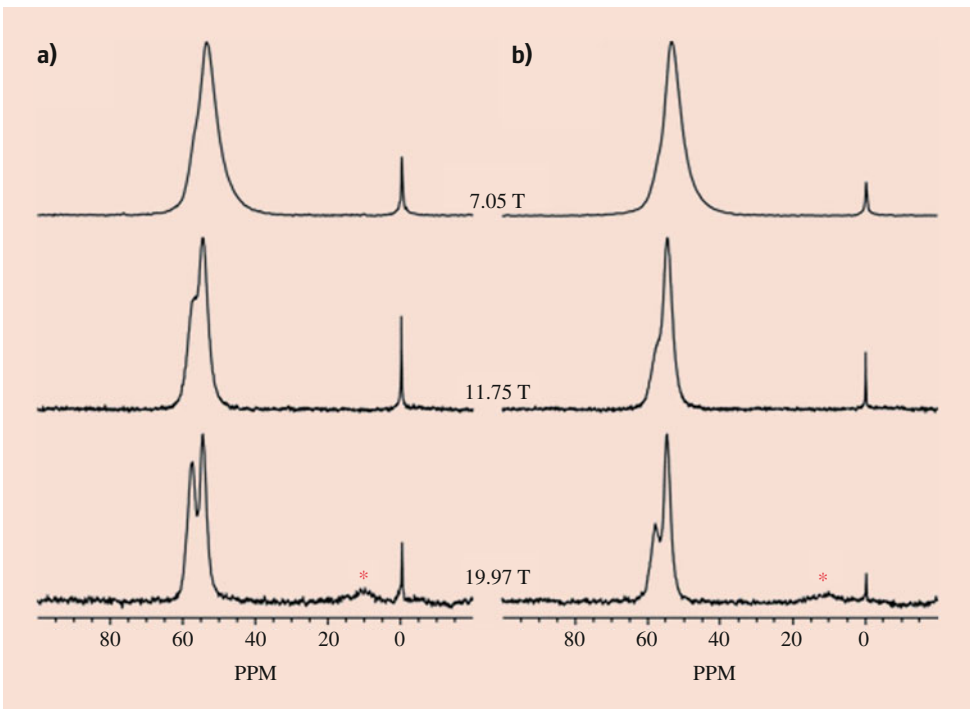

Fig. 34.7 ^{27}Al MAS NMR spectra of HBEA zeolites at magnetic field strengths from 7.05 and 11.75 to 19.97 T: (**a**) HBEA150a and (**b**) HBEA150b. Asterisks denote background signal from the empty rotor. (Reprinted with permission from Hu et al. [34]. Copyright 2017 American Chemical Society)

this represents the current state of the art, 900-MHz magnets are a common high-filed tool and continue to provide unique insight into catalyst systems [37]. As the technological limits of magnetic field strengths continue to be expanded, NMR will increasingly reveal chemical information previously unattainable as a result of the enhanced resolution afforded by ultrahigh fields.

Notably, a 40-T magnet has been employed to reduce the second-order quadrupolar interactions of an aluminoborate sample [38]. This magnet at the National High Magnetic Field Laboratory is a specialized unit and unique in the world, utilizing an 11-T superconducting magnet combined with a 29-T resistive magnet. The aluminoborate sample exhibits large quadrupolar broadening which impedes the detection of all unique ^{27}Al sites due to signal overlap, even at a high magnetic field of 14–25 T. At 40 T, all four ^{27}Al sites were well resolved without peak overlap and lineshapes approaching a Gaussian distribution. Given the unprecedented insight such a magnetic field can offer, it may even be possible to well resolve unique tetrahedral sites in the framework of zeolites in the future.

Figure 34.7 also reveals a key challenge to high-field NMR measurements of solids. At the higher-field strengths, spinning sideband patterns are visible between the two observed signals. This arises from the chemical shift anisotropy being proportional to the magnetic field strength. At these higher fields, the frequency of precession is also enhanced, necessitating faster MAS rates to suppress spinning sidebands as illustrated in Fig. 34.8. At these higher spinning rates, the sidebands are propelled away from the central region of the spectrum, enabling the resolution of multiple sites which would not otherwise be possible as well as magnifying the intensity of the center band. In addition to this, it can be shown from the largely invariant peak position that the primary contribution to this spectrum is the chemical shift tensor and that complete line narrowing is not present due to second-order quadrupolar contributions. Though a uniform site, the trade-offs between the increase in chemical shift anisotropy and the decrease in quadrupolar interactions at high field can be observed in Fig. 34.8. The linewidth (in hertz) increases with field strength, while the apparent linewidth (in ppm) decreases to better resolve the features. Previously published work has described the interplay between these two effects in greater detail [2, 39–41]. Clear advances in magnetic field strength have been recounted, and concomitant improvements to sample spinning rates have been realized as well [42]. Such developments to probe design have enabled sample spinning rates up to ~110 kHz (samples rotated 110,000 times per second). Such rates will effectively suppress the sideband pattern of most nuclei and eliminate strong ^{1}H-^{1}H dipolar coupling, if present in the sample system. While such spinning rates are possible, ~30 kHz is much more accessible and routine for high-field solid-state NMR measurement.

To accurately describe the chemical species of interest with NMR, it is most appropriate to characterize not only the isotropic chemical shift of the nucleus but the full set of chemical shift tensors, the quadrupolar interactions, and the characteristic angles between the two sets of parameters. This is the only true way to accurately characterize a quadrupolar spin via NMR spectroscopy. In practice, it is sometimes not practical to do so given the potential constraints of system, but a true, thorough characterization carefully accounts for each of these parameters.

Efforts to exploit high-field MAS NMR to reveal unique details on catalyst systems will be detailed in the sections below. While detailed reviews have been presented for various nuclei in a variety of applications over the years [43–46], herein, we highlight, ^{27}Al and ^{51}V NMR due to their prevalence and importance to catalysis science. High-field efforts to understand electrochemical reaction systems will also be explored, and commentary on other challenging nuclei will be provided.

34.3 High-Field ^{27}Al MAS NMR

Aluminum is widely abundant in a number of chemical systems. It occurs naturally in a number of minerals and holds great importance in catalysis as transition alumina or in aluminosilicates. Such aluminosilicates constitute a vast majority of the Earth's crust and thus are important also to geochemistry applications. The dominating isotope is ^{27}Al at >99.9%, which is conveniently an NMR-active isotope. This nucleus, however, is quadrupolar with a spin of 5/2, meaning that it will be subject to the quadrupolar effects previously described. As shown for zeolites, sufficiently high fields dramatically enhance the resolution of the spectra enabling multiple sites to arise from one broad feature. The frequency of the central transition is often slightly displaced by second-order perturbations, but the isotropic chemical shift can be approximated with the quadrupolar coupling constant and asymmetry parameter [47]. Typically, such displacements are less than 10 ppm even at a field strength of 12 T and decrease at high field [31]. The typical range of chemical shift for aluminum species spans from 110 to −20 ppm. For catalyst studies, one of the most common features is the tetrahedrally coordinated Al (AlO_4; Al_T) which appear between 50 and 80 ppm. The environment such as nearby ligands and specific structure can shift the location of these signals. For example, AlO_4 Q^3 (3Si) primarily exist at lower field in the 75–80 ppm range, while AlO_4 Q^4 (4Si) typically occupy the 60–75 ppm range. Numerous groups have developed formulations to estimate the Al-O-Al or Al-O-Si bond angles based on the chemical shift [48–53]. These have been

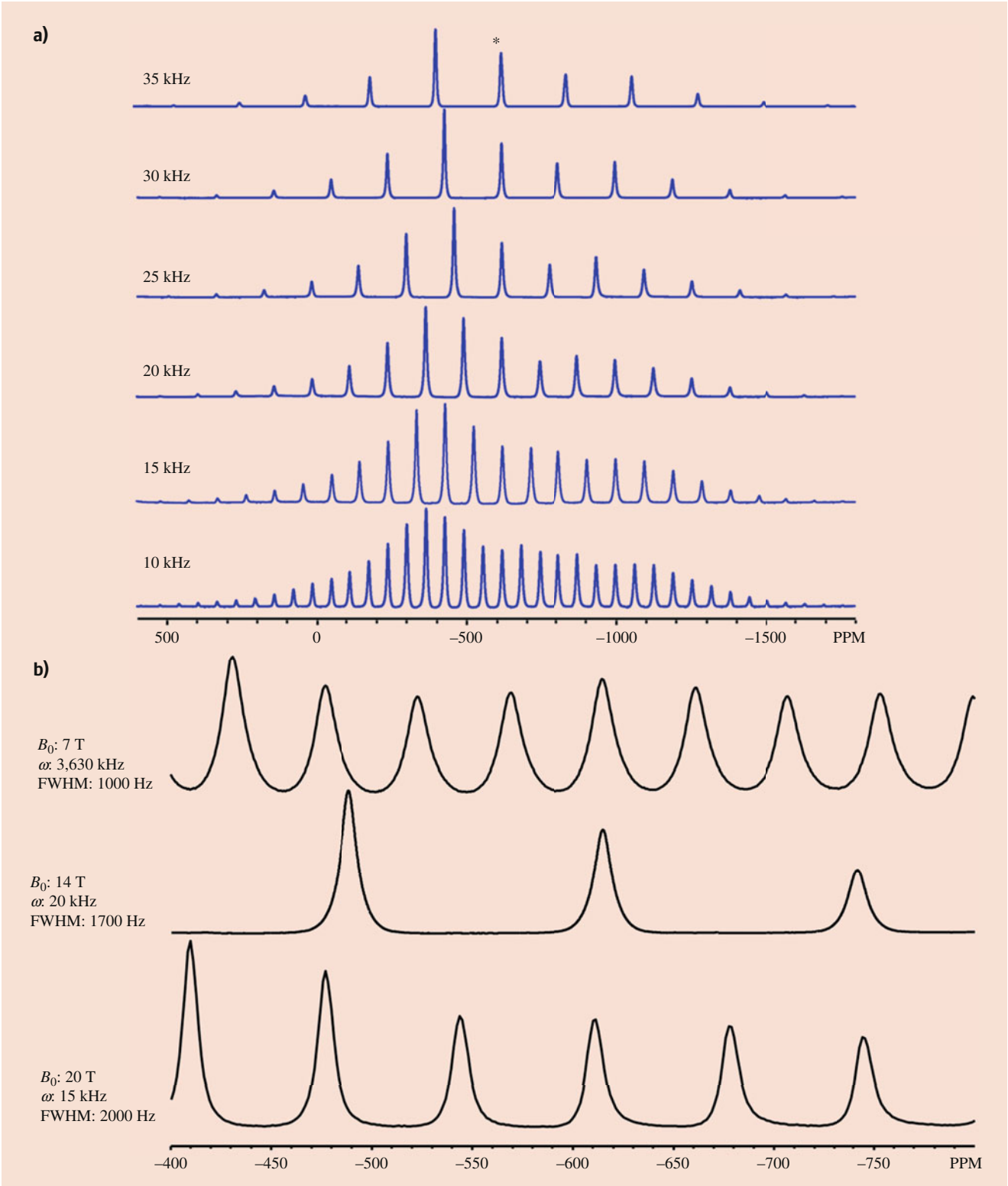

Fig. 34.8 Spinning sideband patterns for bulk V_2O_5 powders under varying spinning rates collected at 600 MHz where * represents the center band (**a**) and V_2O_5 at different field strengths (**b**)

shown to be valid for a limited selection of aluminosilicate frameworks. Pentahedrally coordinated aluminum species (Al_P) are commonly present in the 30–40 ppm region, while octahedral alumina (Al_O), as the hexa-hydrated cation reference, are present from −10 to 20 ppm. The ability for NMR to distinguish and quantify these sites makes it a powerful technique to probe catalysts containing aluminum.

Such a high-resolution capability has enabled the detailed study of important industrial materials such as transition aluminas [54–62]. Though γ-Al_2O_3 is commonly employed for sulfur production and alcohol dehydration, the structural morphology of alumina modulates through a number of polymorphs before reaching the thermodynamically stable α-Al_2O_3 structure. Due to the challenges associated with monitoring the structures of alumina during phase transitions, a clear correlation between reaction rates and ^{27}Al sites was absent. High-field NMR (21 T), however, enables the observation of the aluminum species which are present in the sample [63]. Figure 34.9 illustrates the evolution of such species after treatment from 500 °C to 1300 °C to simulate the extended use in a reaction environment. Significant changes in the Al^{3+} coordination occur during the thermal treatment. Broad peaks at 16, 35, and 70 ppm corresponding to Al_O, Al_P, and Al_T, respectively, are present in all spectra. At elevated temperatures, neat Al_T and Al_O features arise, and a decrease in Al_P species were observed. By quantifying these high-field results, the authors discovered that the abundance of Al_P sites was well correlated with the production of ethylene during ethanol TPSR experiments and ascribed this species as the active center for this important reaction. Not only are such pentahedrally coordinated alumina sites important for reactivity, they have also been found to play a role in supporting other metals onto the surface.

Supported metal catalysts possess a deep pool of applications for catalytic purposes. Such transition Al_2O_3 has also been employed as a support for metal particles and metal oxides. The anchoring positions of such active species on this nonreducible oxide support are of great interest for maximizing the dispersion of the metal. However, such a determination is challenging owning to the need for a clear grasp of the

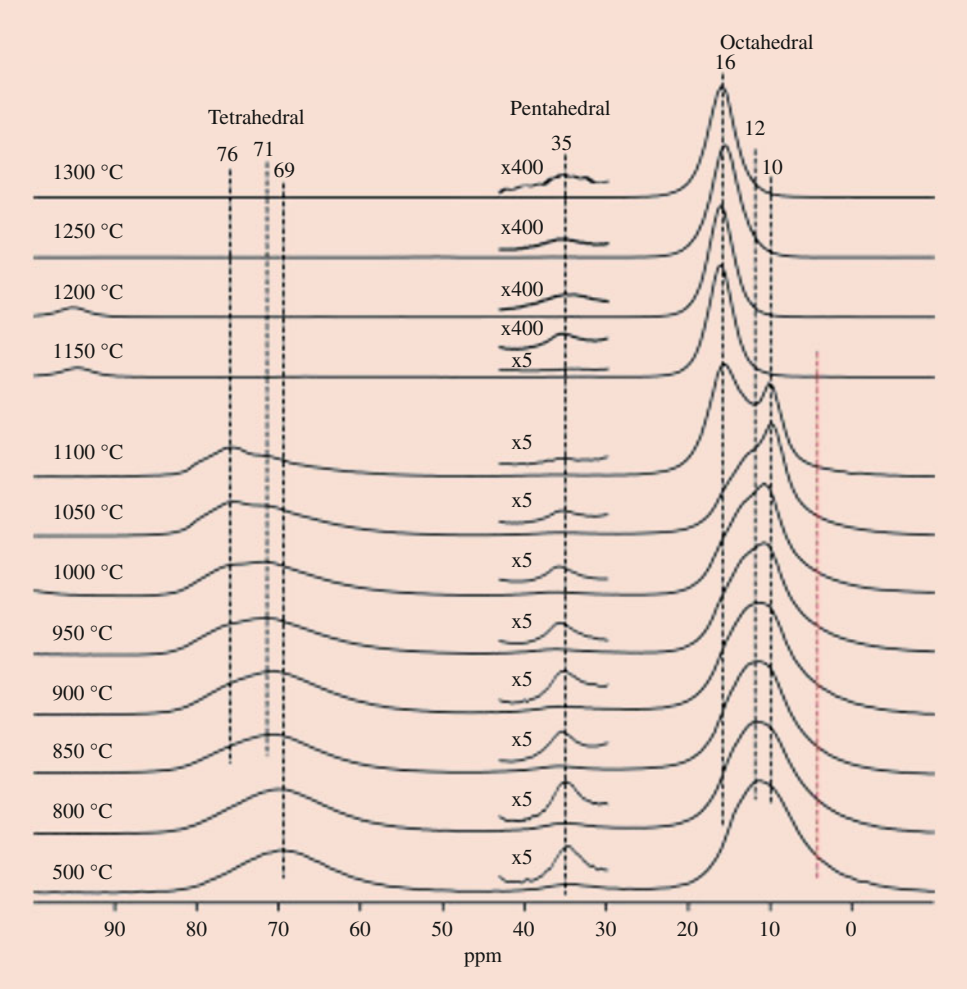

Fig. 34.9 The center band spectra of SP ^{27}Al MAS NMR spectra of samples annealed at different temperatures. The peak at ≥90 ppm corresponds to spinning sidebands. (Reprinted with permission from Hu et al. [63]. Copyright 2016 Elsevier)

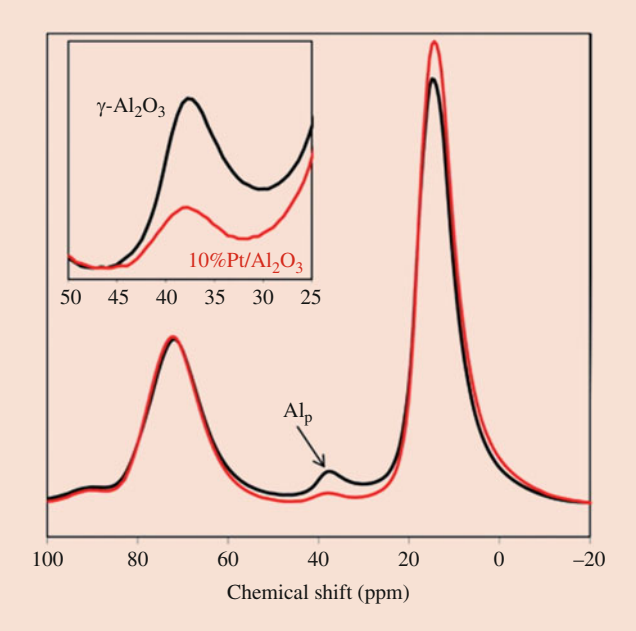

Fig. 34.10 ^{27}Al MAS NMR spectra of γ-Al_2O_3 (black) and 10 wt% Pt/γ-Al_2O_3 (red) (both samples were calcined at 573 K before NMR measurements). (Reprinted with permission from Kwak et al. [64]. Copyright 2009)

surface defect sites. As a supported metal, Pt has been observed to atomically disperse onto the support of the metal oxide. As shown in Fig. 34.10, such an incorporation coincides with a decrease in spectral intensity of coordinatively unsaturated pentahedral alumina sites, the abundance for which the added platinum accorded [64]. Under metal-loading conditions exceeding the quantity of Al_P, two-dimensional PtO islands were observed. This is consistent with observations of tungsten oxide supported on γ-Al_2O_3, whereby seven unique Al sites were observed with the aid of two-dimensional high-field NMR and that Al_P decreased monotonically with the impregnation of tungsten, generating new Al_O sites in place of Al_P [65]. Such assignments were corroborated with computational modeling.

Zeolites are another common catalyst material for which unique molecular insights may arise from characterization by high-field NMR [17, 66–68]. In addition to leveraging high-field single-pulse MAS NMR, MQMAS has been employed to reveal new details regarding the aluminosilicates. ^{27}Al is especially well suited for such two-dimensional MQMAS NMR measurements since this quadrupolar nucleus is relatively sensitive compared to many other nuclei. For representative HBEA zeolites of the same silica-to-alumina ratio, tetrahedral species were shown to primarily resonate near 58.8 and 55 ppm in a range of positions due to the nonuniformity of the nine crystallographic Al T-sites as visible in the isotropic dimension (F1) in Fig. 34.11 [34, 35]. Line fitting of slices parallel to the F2 dimension enables extraction of the isotropic chemical shift and quadrupole coupling constant of the observed species. A distribution of isotropic chemical shifts is apparent for each of the two dominating features at high field. The resulting fitting demonstrated two C_Q values of 2.4 and 1.8 MHz for the feature at 55 ppm and one value of 2.5 MHz at 59 ppm. The extraction of such parameters enabled the deconvolution of the two broad peaks at 60 and 55 ppm from the single-pulse spectra, demonstrating that even zeolites that should contain similar species will likely have a contrasting distribution of Al-occupied T-sites. This demonstrates the importance of high-field measurement in providing a detailed understanding of the specific catalysts in use.

While single-pulse and MQMAS high-field NMR can provide truly insightful descriptions of the catalyst systems, other two-dimensional pulse sequences are able to provide powerful, specific information for a catalyst system. Double-quantum MAS NMR (DQ-MAS) is one such tool employed to approximate the spatial distribution of aluminum species [69]. This technique is challenging for dilute Al species but can be aided by the employment of a high-field magnet [70]. This technique has been successfully demonstrated on samples of zeolite HY which underwent dealumination [71]. The ^{27}Al DQ-MAS NMR spectra of these samples are illustrated in Fig. 34.12. The parent sample exhibits a single Al_T site evidenced by the diagonal autocorrelation peak at 61, 122 ppm. The result illustrates that these framework alumina sites are in close proximity to each other. The progressive dealumination of the parent sample in (A) gives rise to new features in both single-pulse and DQ-MAS NMR spectra. HY-500, for example, reveals a new feature at 0 ppm from the extra-framework Al_O species (the authors note the potential for both AlO and $Al(OH)_3{\cdot}3\ H_2O$). In addition to the autocorrelation features of Al_T and Al_O peaks, cross peaks are observed at 61, 61 and 0, 61, demonstrating spatial proximity between four-coordinate framework alumina and Al_O sites. Further increasing the calcination temperature to 600 °C generates new five-coordinate Al sites at 30 ppm in extra-framework positions [72]. These species are shown to be proximal to both the four- and six-coordinate Al species. The strong intensity between four- and five-coordinate cross-peak pairs suggests that these species are of particular close proximity. Upon further increasing calcination to 700 °C, the Al_T species becomes asymmetric and broad from the appearance of a new feature at 55 ppm (four-coordinate extra-framework alumina) and a new cross-peak pair forms at (55, 87) and (32, 87) which shows the close proximity of the $AlOH^{2+}$ (generated by the elimination of water) and Al_P; however, now, spatial correlation with Al_O existed for the new Al_T site. Based on these detailed findings, coupled with single-pulse ^{27}Al, ^{1}H, and ^{29}Si, and triple-quantum MAS NMR coupled with computational modeling, the authors proposed a scheme to describe the dealumination mechanism of HY zeolite.

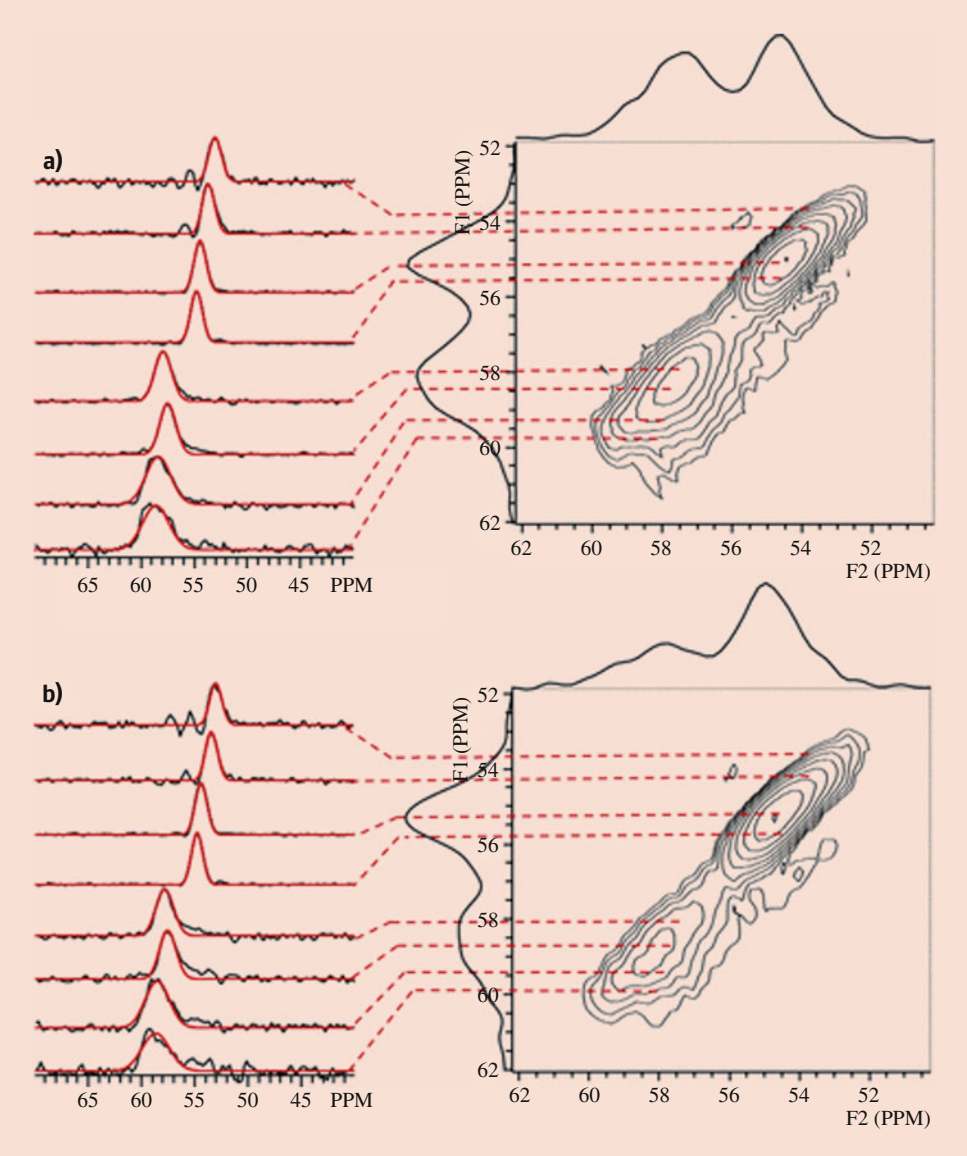

Fig. 34.11 ^{27}Al MQMAS NMR spectra of HBEA zeolites on the right and the representative slices (black) parallel to the F2 (acquisition) dimension at selected F1 (the isotropic chemical shift) dimensions with the fitting lines (red) on the left: (**a**) HBEA150a and (**b**) HBEA150b. No line broadening was applied before Fourier transformation in both F2 and F1 dimensions. (Reprinted with permission from Hu et al. [34]. Copyright 2017 American Chemical Society)

34.4 Vanadium Oxide Characterization

Vanadium was isolated as a component of vanadinite and described by Andrés Manuel del Río in 1801. Vanadium represents an important material for myriad applications, most abundantly employed as an additive used in steel manufacturing [73]. Vanadium is also employed for its redox properties since it readily cycles between various states of oxidation both as a solid and in solution. Such electronic states manifest themselves optically, e.g., $[V(H_2O)_6]^{2+}$ (violet), $[V(H_2O)_6]^{3+}$ (green), VO^{2+} (blue), and VO_2^{+} (yellow). The pentavalent state holds the most commercial prominence as the V(V) oxide V_2O_5. This material holds great importance for the production of sulfuric acid through oxidation of SO_2 to SO_3 (contact process) [74]. Vanadium oxide catalysts are employed for a large number of other chemical processes, spanning reactions such as the selective oxidation of paraffins, olefins, and alcohols [75], nonoxidative and oxidative dehydrogenation of alkanes [76], selective catalytic reduction of NO_x [77], oxidation of a wide variety of other organic chemicals [78], and sulfur oxidation [79]. Vanadium oxide catalysts occupy homogeneous configurations and have been characterized with ^{51}V liquid-state NMR, such as those for alkane, alkene, aldehyde, and ketone oxidation reactions. They have also been supported as heterogeneous active sites or within enzyme formulations [80–83]. Metal oxide catalysts generally provide complex catalyst materials, in particular when anchored to a support, owning to the wide array of molecular structures (i.e., monomer, dimer, oligomer,

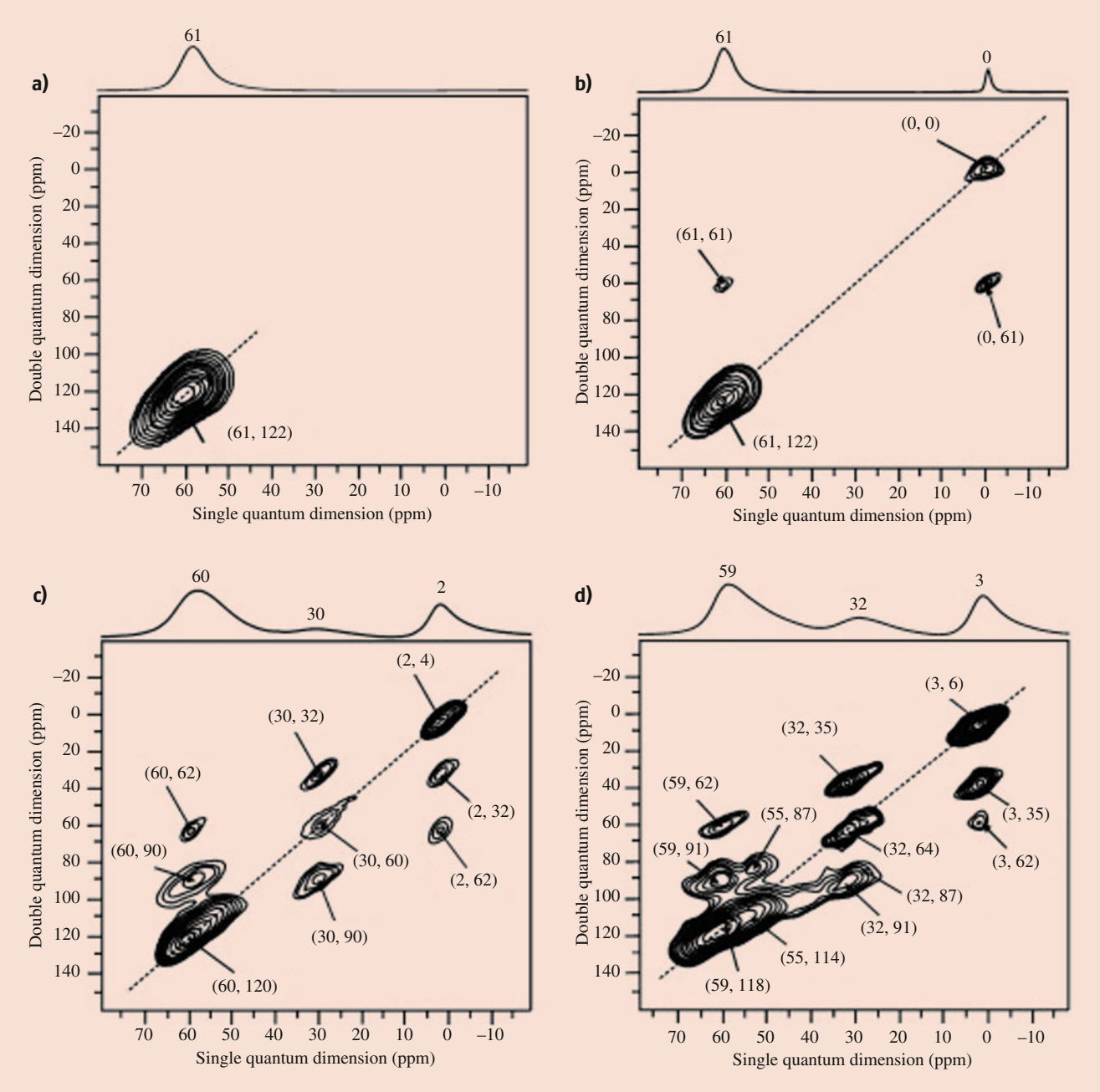

Fig. 34.12 ^{27}Al MAS and DQ-MAS NMR spectra of (**a**) parent HY, (**b**) HY-500, (**c**) HY-600, and (**d**) HY-700 zeolites. One-dimensional ^{27}Al MAS spectra are plotted on top of the two-dimensional ^{27}Al DQ MAS spectra. All spectra were recorded on hydrated samples at 18.8 T with a 3.2 mm probe at a sample rotation rate of 21.5 kHz. About 45 h were required to record one ^{27}Al DQ-MAS NMR spectrum. (Reprinted with permission from Yu et al. [71]. Copyright 2010 Wiley-VCH Verlag MgbH & Co)

polymer, and bulk) which may be present in varying oxidation states. Due to these complexities, an accurate assessment of the active site for these materials is often very challenging to identify, necessitating detailed characterization to address this important and challenging topic.

Heterogeneous catalysts use numerous support materials such as zeolites, molecular sieves, bilayered or co-precipitated mixed oxides, and pure metal oxides. The selection of the support is known to alter the catalyst function and can provide unique advantages compared to the bulk V_2O_5 phase [75]. Supported vanadium oxide materials undergo reduction of the active V^{5+} centers to the V^{4+} state and can be reoxidized during a catalytic cycle to restore the initial catalyst function. The V^{5+} oxidation state is diamagnetic, containing only paired electrons and making ^{51}V MAS NMR spectroscopy an attractive option for characterization.

The most abundant vanadium nucleus (^{51}V: 99.75%) is conveniently an NMR-active nucleus, though it is quadrupolar with a spin 7/2 and short relaxation times. Vanadium also typically hosts fairly low quadrupolar coupling where chemical shift anisotropy can be the more relevant factor in determining lineshape. Though it has these advantages, it is also challenged by typically low abundance in catalyst samples (~1%) which, in addition to limiting the detection, also decreases symmetry and enhances quadrupolar effects, making detection of broad features more challenging and encouraging the use of high-field NMR to prove the materials. ^{50}V is also an NMR-active, with a natural abundance of 0.24% and spin 6, but suffers from poorer sensitivity and very broad lines when compared to ^{51}V [84]. Previous work has extensively investigated the NMR parameters for numerous vanadium compounds, providing some basis for comparison of the observed signals to a reference compound [85, 86]. A nice summary of these parameters as they pertain to ^{51}V MAS NMR is available in the *Encyclopedia of Nuclear Magnetic Resonance* [39].

On the surface of the catalyst, vanadium oxide resides in molecular configurations ranging from isolated VO_4 units to bulk-like V_2O_5 crystallites. Decavanadate structures have also been observed [87]. As a supported oxide, vanadium oxide conformations typically evolve from monomeric, distorted tetrahedral with one V=O and three V-O-support bonds at low surface densities through larger polymeric networks at moderate loadings to V_2O_5 crystallites when the monolayer is exceeded. Specific structural insights can be provided by NMR which are not available by other means of characterization. The spectral assignments of various ^{51}V species supported on titanium dioxide, a common support, have evolved over time as better descriptions of the system have emerged. Computational modeling has played a key role in refining the assignments of these species, where simulations of surface structures and chemical shift calculations are directly employed. Since titania-supported vanadium oxides are a critical focus for applications such as emission controls, reported assignments for various spectral features have been summarized in Table 34.3. It should be noted that assignments by computational modeling of the nuclei are ideally compared on the basis of multiple experimentally measured attributes such as isotropic chemical shift, quadrupolar coupling constant, and asymmetry and not one parameter alone to enhance the reliability of such assignments.

As a quadrupolar nucleus, ^{51}V is impacted by severe broadening at low magnetic fields. Shown in Fig. 34.13, at low magnetic fields, some supported vanadium oxide catalysts reveal very broad features that cannot be well resolved due to the distribution of isotropic chemical shifts and the notable quadrupolar coupling constant [94, 95]. State-of-the-art technology enabling high magnetic fields and fast

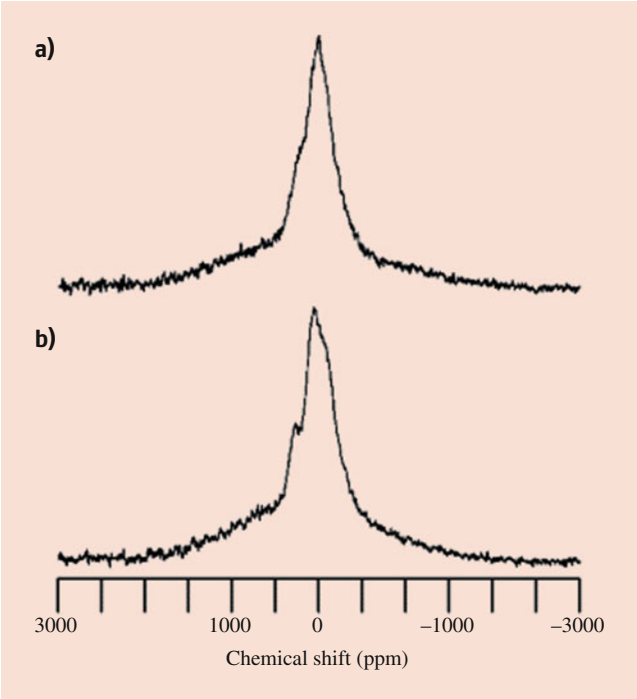

Fig. 34.13 ^{51}V MAS NMR spectra obtained on the VOx/TiO2/MCM-41 sample at two different spin rates of (**a**) 10 kHz and (**b**) static. The spectra are referenced to the center band of V_2O_5 at 0 ppm. (Reprinted with permission from Kwak et al. [94]. Copyright 2006 Elsevier)

Table 34.3 Reported species identification of ^{51}V NMR signals of titania-supported vanadia catalysts

Ref.	−502	−510	−530	−555	−587	−610	−630	−650	
[88]		Dist. octa.	Dist. octa.	Tetra. poly.		V_2O_5			Poly. octa.
[89]		Octa.	Tetra.						
[90]						V_2O_5		Dist. octa.	Poly. octa.
[91]		Trigonal pyramid		Dist. tetra.		Dist. octa. (trigonal bipyramid)			
[92]	Tetra. monomer		Monomer	Double-bridge dimer	Dimer/ poly.	V_2O_5	Single-bridge dimer and poly.	Poly.	
[93]	Tetra. monomer		Octa. monomer	Dimer	Dimer/ poly.	V_2O_5-like	Poly.		

Dist. distorted, *octa.* octahedral, *tetra.* tetrahedral, *poly.* polymer

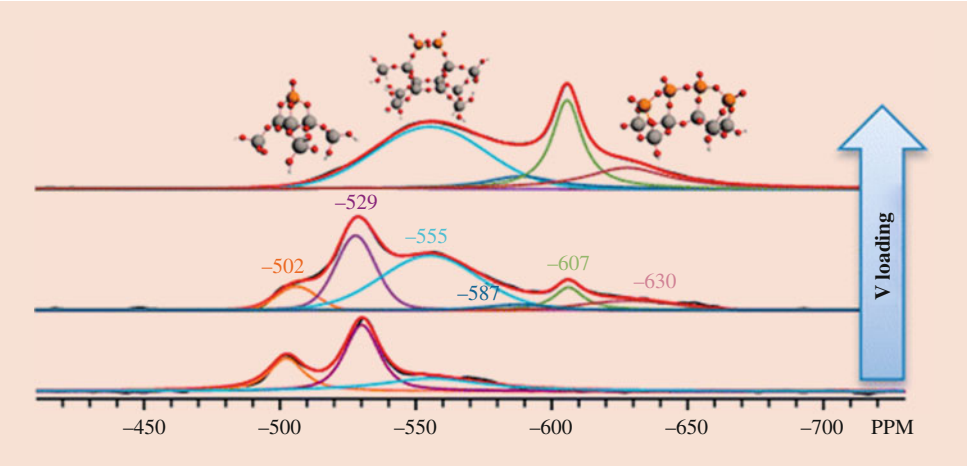

Fig. 34.14 51 V MAS NMR spectra at 20 T and 55-kHz MAS rates of 0.2, 0.9, and 5% V_2O_5/TiO_2 (bottom to top). (Reprinted with permission from [92]. Copyright 2015 American Chemical Society)

spinning rates, however, can offer enhanced spectral resolution as well as suppress spinning sidebands, enabling the observation of unique vanadium oxide environments [92]. This was exemplified in a 2015 study from *ACS Catalysis* which employed a 20-T magnet and fast spinning rates of 55 kHz. The results of this study are shown in Fig. 34.14 which reveal the evolution of ^{51}V signals as the loading of vanadium oxide is modulated. They also highlight the advantages of high-field detection at fast spinning rates when compared to catalysts collected at lower magnetic fields, wherein enhanced spectral resolution is possible which better resolves unique vanadium oxide species [96]. At low vanadia loadings, NMR could identify and quantify such surface species as monomeric(−500 and −530 ppm) and dimeric (−555 ppm) when coupled with computational modeling. The relative abundance of these species was modulated by the surface density of vanadium oxide introduced. At an enhanced loading of 0.9% V_2O_5, the catalyst exhibited an increase in intensity, including the growth of dimeric vanadia and the appearance of oligomeric species at −587, −607, and −630 ppm. These features further grew at the expense of monomeric vanadia in the 5% V_2O_5 catalyst material. Such an investigation provided the first clear speciation of titania-supported vanadium catalysts and enabled an evidence-based speculation on the active sites for the oxidative dehydrogenation of methanol. Strong correlations could be drawn between the activity of the catalysts and the presence of monomeric vanadia at −500 and −530 ppm as well as with dimeric species at −555 ppm. The high-field measurement provided unprecedented insight into the speciation of vanadium oxide on the catalyst surface, enabling the detailed analysis of the active structures for reactivity.

Vanadia-based selective catalytic reduction (SCR) is an important reaction for the abatement of polluting nitrogen oxides in which high-field NMR has provided detailed insight. For this industrial application, the catalyst surface is typically modified with a promoter such as tungsten or molybdenum oxide. The mixture of surface oxide species introduces complications when trying to understand the structure of the active center with techniques such as UV-vis where band overlap prevents an estimation of the oligomeric fraction of vanadium. However, the atom-specific nature of NMR enables the observation of the molecular structures of vanadia in the presence of these promoters. To determine the potential effect of such tungsten oxide promoter on the structure of vanadia, samples with contrasting quantities of vanadia and tungsten were prepared and analyzed with ^{51}V MAS NMR. The results (Fig. 34.15) show a similar evolution in vanadia speciation with increased tungsten oxide loading as with an increased vanadium oxide loading, namely, the enhancement of signals associated with oligomeric vanadia. This was used to show the strong correlation between oligomerized vanadia and the SCR reaction rate. This was explained by the formation of oligomerized vanadia structure at high vanadium oxide loadings or with tungsten oxide present as a promoter which facilitates the SCR reaction through a two-site mechanism. Such an example shows how high-field NMR can be used to solve complex mixed metal oxide catalysts to reveal the active species and mechanism of promotion.

Though significant efforts and advances have been made to identify the surface structures of titania-supported vanadium catalysts at high field, not all supports enable such detailed findings. Silica-supported vanadium oxide catalysts, for example, have long been the subject of debate as to the surface structures present. Other characterization techniques have suggested the possibility that silica can only support isolated vanadium species on the surface. High-field NMR typically resolves only one or two broad environments as shown above, whose identity is speculated primarily based

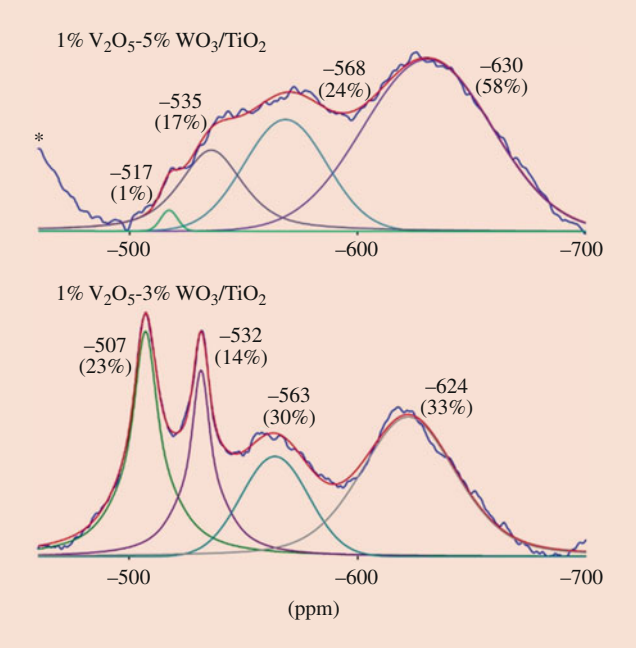

Fig. 34.15 ^{51}V MAS NMR spectra of 1% V_2O_5-(3–5)% WO_3/TiO_2 catalysts prepared by incipient wetness impregnation and dehydrated. Spectral deconvolution summation is presented by the red line; the collected data are shown in blue. (Reprinted with permission from [93] Copyright 2019 Wiley-VCH Verlag GmbH & Co)

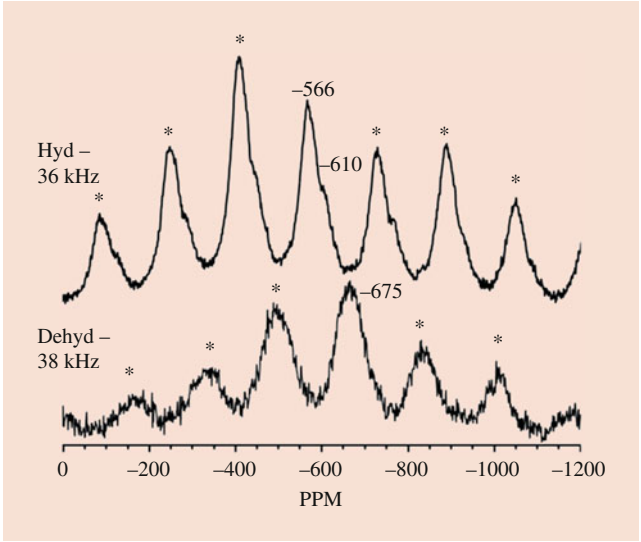

Fig. 34.16 Solid-state ^{51}V MAS NMR of supported 8% VO_x/SiO_2 under hydrated (36 kHz) and dehydrated (38 kHz) conditions. Hydrated catalysts contain a major peak at −566–67 ppm and a shoulder at −610–13 ppm, and dehydrated catalysts exhibit a major peak at −675 ppm. *denotes spinning sidebands. (Reprinted with permission from Jaegers et al. [101]. Copyright 2017 American Chemical Society)

on known references [97–101]. One recent investigation explored the potential structures of hydrated and dehydrated materials and found one broad site at −675 ppm for dehydrated materials and two sites at −566 and −610 ppm for hydrated materials as shown in Fig. 34.16 [101]. Coupling previous results with computational modeling suggested that in the dehydrated case, the broad peak was likely to arise from isolated monomeric vanadia species, but the chemical shift from dimeric and cyclic trimers should be similar to the monomer, highlighting the challenging of characterizing silica-supported vanadia species. The hydrated state was similarly ascribed to monomeric or dimeric species which experience support bond hydrolysis(−566 ppm) or oligomerization to bulk V_2O_5 crystallites(−610 ppm). Efforts to reveal the chemical environments of such species have manifested themselves in the form of quadrupolar parameter extraction from the spinning sideband patterns at high field [102]. Though this represents an advance in the detailed analysis of spectra, more work is necessary to reveal the true nature of silica-supported materials. As NMR technology advances, MQMAS on ^{51}V may become more routine and enable such detailed information.

Two-dimensional ^{51}V NMR has been explored and provides unique information on the system allowing the determination of quadrupole coupling parameters [103]. Such efforts are challenging, even at high field, for supported vanadium oxide catalysts for which single-pulse spectra may take several days to collect. An example of such efforts of a vanadia catalyst spray-dried with phosphorus to generate surface complexes on titania revealed a single feature with an isotropic chemical shift near −755 ppm [104]. Such 3QMAS and 5QMAS spectra are replicated in Fig. 34.17, where the isotropic, anisotropic, and quadrupolar-induced shifts are designated on the lines. The results suggest that the V-P-Ti sites are likely tetrahedral in coordination with strong distortions from the second coordination sphere causing nonuniformity in the sample. Though much room for improvement exists in the application of such measurements to catalyst systems, these are likely to become more routine as NMR technology continues to improve.

34.5 Energy Storage

Similar to applications in catalysis, the studies of materials employed in energy storage and electrochemical conversions have been propelled by the utilization of high-field magnets in NMR spectroscopy. Such efforts have encompassed testing energy storage components ex situ as well as in situ observation of the system to generate a clear depiction of the chemical transitions that occur on the surface of the electrodes [8]. In direct concert with investigations into catalytic materials, limitations from the low abundance of active

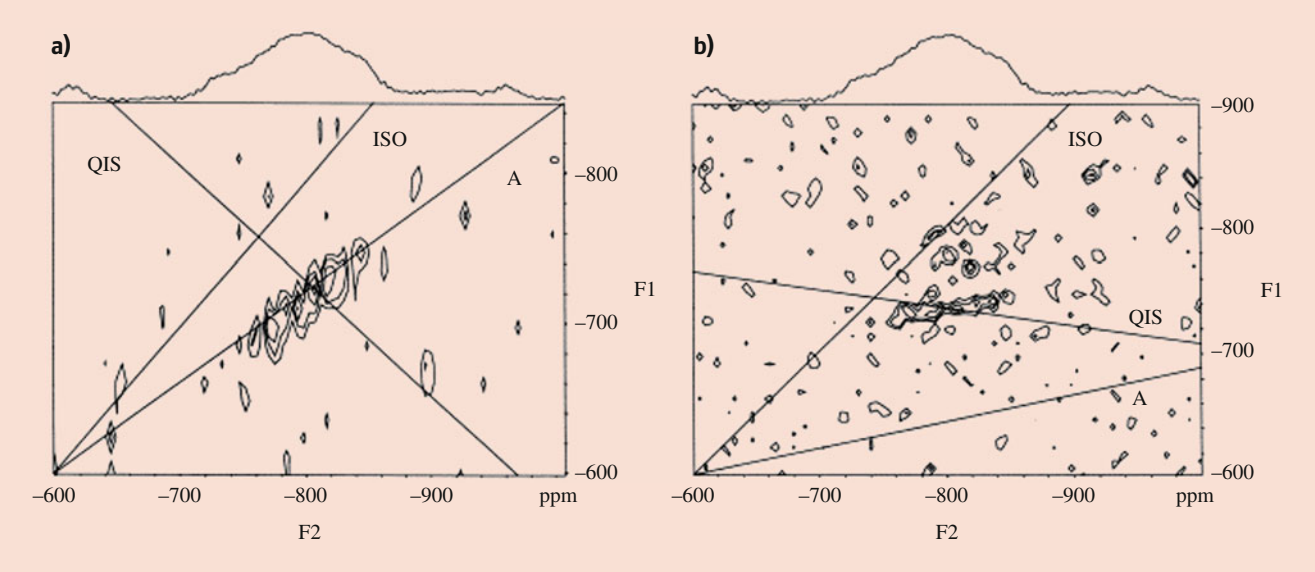

Fig. 34.17 2D ^{51}V 3QMAS (**a**) and 5QMAS (**b**) spectra of VO_x/TiO_2 catalyst containing 10 wt% P_2O_5. Isotropic (ISO), anisotropic (A), and quadrupolar-induced shift (QIS) axes are marked. (Reprinted with permission from Lapina et al. [104]. Copyright 2000 Elsevier)

nuclei and poor resolution of electrochemical species at relevant concentrations are rectified by the employment of high-field NMR. A clear example of this comes from studies of hydrogen storage in the form of lithium hydride (LiH) [105]. As depicted in Fig. 34.18a, a dramatic difference in the resolution of the ^{6}Li spectrum is attained by tripling the magnetic field strength. At the 7 T field, only a single peak with an approximate Gaussian lineshape is visible. This broad peak resolves to three unique environments at a magnetic field of 21 T, enabling the identification of distinct lithium species, namely, a feature at 0.0 ppm ascribed to $LiOH{\cdot}H_2O$, another at 2.7 ppm for LiH, and shoulder peak present at 1.1 ppm assigned as LiOH. Using the high-field magnet, the evolution of these species was followed throughout the high-energy milling process.

Spectrum a from Fig. 34.18b represents a commercial $LiNH_2$ consisting of a main feature at 2.6 ppm (crystalline $LiNH_2$) and a shoulder at 1.4 ppm ($LiNH_2H_2O$, validated by the addition of water in a1). The sample was subjected to various treatments to understand mechanical activation of the sample and the release of energy in the form of hydrogen. The LiH powder (b) was milled at room temperature for 45 min (c), which instigated the formation of LiOH (1.1 ppm) and $LiOH{\cdot}H_2O$ (0 ppm) and shifted the LiH species to 2.7 ppm due to changes in the local environment induced by milling. A mixture of $LiNH_2$ and LiH was progressively milled and measured at discrete intervals. The results indicate a reduction in the 2.7 ppm feature from $LiNH_2$ and an increase in a broad peak at 2.0 ppm that is ascribed to an altered defect structure of LiH. Additionally, a shoulder at 1.5 ppm appears as well as the 0 ppm feature indicative of $LiOH{\cdot}H_2O$. The culmination of the results enabled the findings that high-energy ball milling facilitates upfield shift of the resonances in ^{6}Li MAS indicative of increases to the average local electronic shielding around Li and that milling causes interactions between $LiNH_2$ and LiH. Additional milling time increases the intensity of the 2.0 ppm peak, which may be due to an increasingly defective lattice on the surface of $LiNH_2$ and LiH. Lower milling temperatures exhibit a similar effect, suggesting that lower temperatures are more efficient for mechanical activation than room temperature. Such detailed insights on the structure of LiH species and the release of hydrogen were only possible due to the advantages afforded by high-field NMR.

In addition to hydrogen storage, high-field solid-state MAS NMR is a key tool to understand the solid-electrolyte interface (SEI) composition for electrochemical energy storage. Such examples include the use of ^{6}Li MAS NMR to study the electrodes and SEI formed in lithium batteries [106–108]. At a high field, the composition of the SEI formed in Cu-Li cells was determined by employing a multinuclear strategy involving ^{1}H, ^{6}Li, ^{13}C, and ^{19}F. The 20 T field afforded sufficient resolution to enable the deconvolution of at least six unique lithium species present in SEI layers harvested from cells with contrasting electrolyte components. One such species was metallic Li, which is often regarded as dead Li species. This species, unable to contribute to electrochemical cycling, was found in contrasting abundance among the various electrolyte configurations. The findings enabled by high-field detection have implications on the safety and performance of such galvanic cells. For example, the detected LiF species (regard as a good Li^+ conductor) was observed only at specific lithium bis(trifluoromethanesulfonyl)imide (LiTFSI) concentrations in the electrolyte. A quantitative

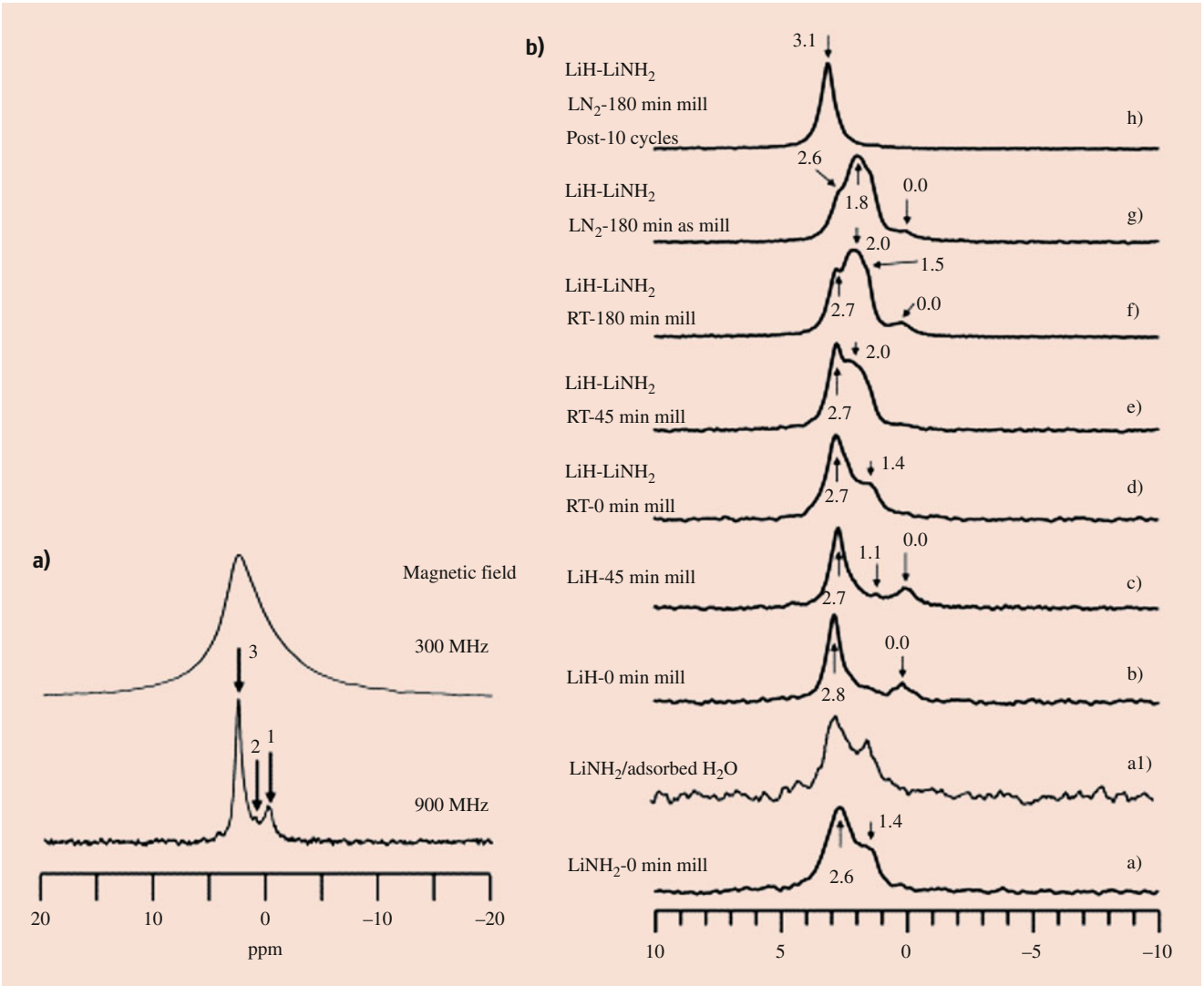

Fig. 34.18 (**a**) ^{6}Li MAS NMR spectra of solid powder LiH sample that was ball milled for 45 min at room temperature. The top trace was acquired on a 300 MHz NMR spectrometer at an MAS rate of 5 kHz ($\delta\upsilon_{1/2}$ = 4.75 ppm or 210 Hz). The bottom trace was acquired on a 900 MHz spectrometer at a sample spinning rate of 18 kHz. (**b**) ^{6}Li MAS spectra acquired with ultrahigh magnetic field of 21.1 T and at a sample spinning rate of about 18 kHz. (Reprinted with permission from Hu et al. [105]. Copyright 2008 Elsevier)

account of the species specificity on the solid material provides truly unique and explicit insight into the underlying surface chemistry. Not only are solid species used in battery applications benefitted by strong magnetic fields, but liquid samples experience enhanced resolution and sensitivity as well.

The natural abundance detection of low-concentration species in energy storage solvents is yet another area in which high-field detection has greatly propelled a molecular description of the chemical system. For example, high-field ^{17}O and ^{6}Li spectra have been employed to understand the solvation structures of electrolytes for electrochemical applications. The high and enhanced resolution afforded by the field strength enabled the detection of ^{17}O at natural abundance in low-oxygen abundance systems. ^{17}O is not only challenging to observe in numerous chemical systems owing to its strong quadrupolar coupling (I = 5/2) but in particular due to its low natural abundance of 0.038%. Consequently, even enrichment of chemical species to attain detection is hindered by the high cost of isotope-specific compounds. Despite this, the solvation structures for LiFSI (DME) (LiFSI dissolved in 1,2-dimethoyethane) could be resolved on the basis of chemical shift coupled with computational modeling to show the modulation of TFSI coordination with concentration [109]. Figure 34.19 illustrates one such example of high-field ^{17}O which exemplifies the range of oxygen environments present in such solutions and how concentration modulates their abundance and speciation. In this study, LiTFSI was dissolved in a number of solvents at a range of concentrations to form an electrolyte [110].

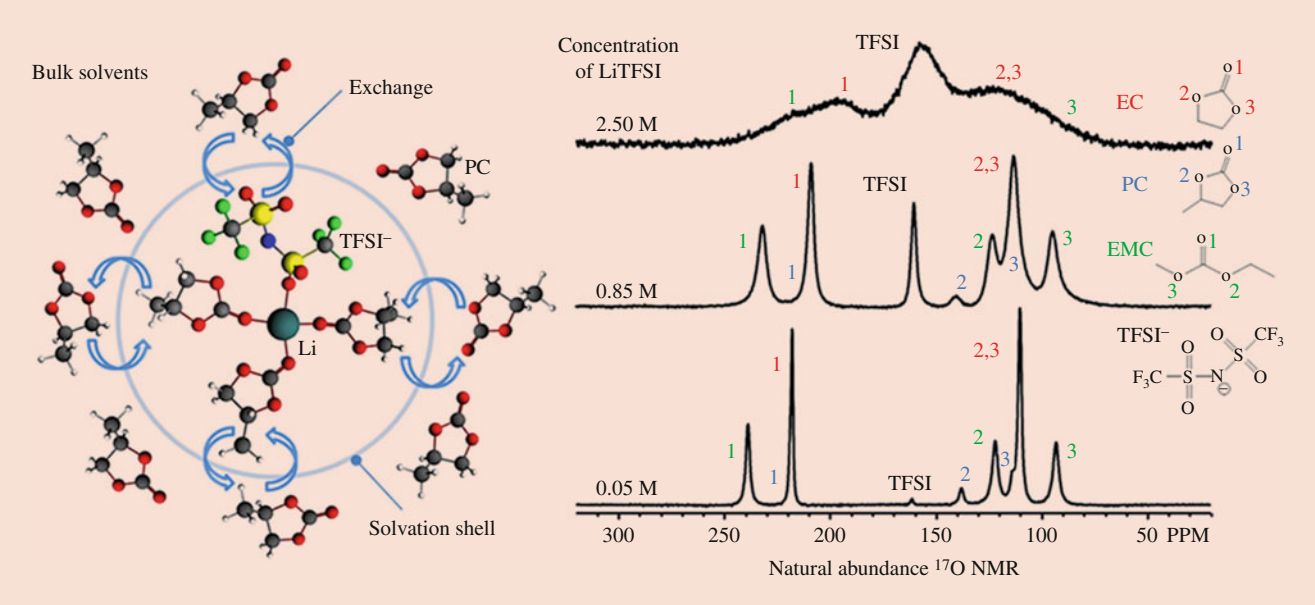

Fig. 34.19 High-resolution observation of natural-abundance ^{17}O NMR for electrolyte solutions at low to high concentrations and the accompanying exchange of chemical species. (Reprinted with permission from Deng et al. [110]. Copyright 2015 Elsevier)

Carbonyl displacement was observed more strongly than oxygen in ether positions with the changing formulation, highlighting the importance of clearly resolving this feature. As such, TFSI was proposed as the species directly interacting with the Li^+ cation. The results enabled the determination of the coordination around Li^+ and showed that the first coordination sphere is comprised of four carbonyl species interacting with Li^+. In excess solvent, quick exchange is observed between coordinating oxygen-containing species and solution-state species. ^{17}O has also been employed to look at the cathode materials and observe the paramagnetic shift to better understand the delithiation process. Such experiments enable the electrochemical cycling process of Li-based batteries to be monitored [111].

A somewhat similar approach has been employed to provide insight on solvation structures around ^{25}Mg cations, important for the potential alternative Mg-based battery technology [112–114]. To propel this next-generation research, it is important to understand the limitations in cell formulation which lead to poor performance. High-field NMR explored the solvation structures and dynamics of electrolyte salts Mg $(BH_4)_2$ (magnesium borohydride) and $Mg(TFSI)_2$ dissolved in diglyme at various concentrations and ratios to reveal that mixtures of the two salts decrease the strong interactions with BH_4^-, resulting in increased coordination of Mg^{2+} with solvent molecules. The likely solvation structures of these species were proposed with the assistance of computational modeling for each condition. Such results highlight the power of high-field NMR to provide unique and specific insight into the underlying chemistry of applications that employ challenging nuclei.

34.6 Low-Natural Abundance, Low-Gamma Nuclei

Since the criteria for the suitability of an element for NMR are (1) possessing nuclear spin and (2) consisting of a diamagnetic electron configuration, it would follow that most elements can be probed with NMR spectroscopy, enabling detailed insight into the abundance of catalyst systems. However, the sensitivity of many of these nuclei suffers from either poor natural abundance, low-γ, or a combination of both. In solid-state NMR, detection of low-γ nuclei is challenged by their inherently poor sensitivity. Many of these nuclei hold great importance to catalysis as the active metal species, such as ^{25}Mg, ^{47}Ti, ^{49}Ti, ^{67}Zn, ^{91}Zr, ^{95}Mo, ^{97}Mo, ^{105}Pd, ^{107}Ag, ^{109}Ag, ^{183}W, ^{195}Pt, etc., and reviews devoted solely to [115] a given nucleus are readily available [44, 45, 115–119]. A number of other chemical species may be present on the catalyst which impacts the reactivity of the material as either a poison or promoter. These species may contain nuclei that also suffer from poor sensitivity due to a low-γ. This includes nuclei such as ^{14}N, ^{33}S, ^{35}Cl, ^{37}Cl, ^{39}K, and ^{43}Ca. Since the sensitivity of these species is proportional to both B_0 and γ^3, one strategy to enable the detection of these nuclei is to employ high-field NMR.

A number of these nuclei are commonly present in metal oxide catalysts. Such nuclei as ^{25}Mg, ^{47}Ti, ^{49}Ti, ^{67}Zn, ^{91}Zr, ^{95}Mo, ^{97}Mo, and ^{183}W are employed as active species, promoters, and supports; many of these elements have been previously mentioned in this summary. However, their observation is hindered by poor sensitivity and often broad

features. A few applications will be mentioned below for the reader's interest. For example, ^{25}Mg is an important element for numerous chemical transformations (as briefly mentioned in the previous section). It suffers, however, from severe quadrupolar broadening in asymmetric environments. For catalytic applications, the oxide form MgO is of greatest relevance. Despite the severe quadrupolar broadening experienced in some minerals, the symmetric environment of MgO leads to sharp resonances at 25–27 ppm but experiences long relaxation times on the order of minutes [120–122]. Recent work at 20 T has highlighted insights for the synthesis of $MgCl_2$ Ziegler-Natta catalyst for olefin polymerization and shown the response of the ^{25}Mg and ^{35}Cl NMR spectra to an extended surface area [123]. Both ^{25}Mg and ^{43}Ca, in conjunction with ^{17}O, have been used to observe the paramagnetic shift of dopants such as NiO and CoO incorporated into MgO and CaO materials [124]. The presence of these dopants shifted portions of the uniform spectra for the pure oxide to varying degrees based on the concentration of the dopant and the proximity of the paramagnetic species.

Due to the extensive industrial use of TiO_2-based catalysts, their observation by NMR is of great interest to researchers. There are two magnetically active titanium isotopes, ^{47}Ti and ^{49}Ti, with quadrupolar spins of 5/2 and 7/2, respectively. Both have a low natural abundance and resonance frequency. Their frequencies are uniquely similar such that their spectra sometimes overlap [125]. As a representative application, metal organic framework (MOF) materials have been investigated with ^{47}Ti and ^{49}Ti NMR, where the signals were shown to be sensitive to molecules present in the MOF pores [126]. Further, examples of high-field NMR to understand the phases of titanium phosphates or titanium silicates have been reported to provide unique, structural insight [127, 128]. ^{67}Zn is a quadrupolar isotope of another prominent metal oxide that suffers from low sensitivity. As high-field spectroscopy becomes more prominent, its spectroscopic observation has played an increasing role in understanding the nature of Zn sites and coordination on the oxide surface [129, 130]. Finally, ^{91}Zr is another isotope for a common metal oxide material which has been the subject of detailed review [119]. Though it suffers from a very large quadrupole moment, the nucleus has been successfully resolved to reveal the local environment in MOF and phosphate applications [117, 126].

^{183}W is infrequently reported due to the lower receptivity and extended relaxation times. Such signals have been collected for tungsten oxide and tungsten-containing polyoxometalates, however. Two resonances are visible at moderate field in the case of crystalline WO_3 at −414 and −438 ppm due to the crystallographic ally inequivalent species [131]. $H_3PW_{12}O_{40}$ reveals a single resonance with a large chemical shift anisotropy. High-field ^{183}W and ^{95}Mo studies of other polyoxometalates (Lindqvist, Keggin, Keplerate, and Dawson) have revealed the unique and specific NMR parameters for the solid-state spectroscopy of such species [132]. ^{95}Mo likewise suffers from quadrupolar broadening a low-γ and low natural abundance. The quadrupole coupling of various molybdenum-containing compounds has been the subject of detailed attention [116]. While the study of ^{95}Mo species anchored in zeolites for methane dehydroaromatization does not reveal such sharp ^{95}Mo features, it does provide some unique insight into the bonding environments of Mo in the framework [133, 134]. This work took advantage of the contrasting spin-lattice relaxation times between supported Mo species and those in the oxide crystallite to differentiate exchanged Mo from the oxide agglomerates. The results demonstrated a linear correlation between the extent of exchange and the reaction rate and indicated the saturation loading of 0.5 Mo/Al in the MFI framework while providing unique, high-field spectra of the oxide powder.

Noble metals also hold a great importance for catalysis, but such species are relatively unexplored. A number of studies have investigated the spectra of ^{105}Pd, ^{107}Ag, ^{109}Ag, and ^{195}Pt NMR, but these come primarily from investigation into the chemical structure of other materials such as glasses and superconductors with only a modest selection pertaining to catalysis [31, 135–137]. A few demonstrations exist of these nuclei contained within catalyst systems. For example, ^{109}Ag has been explored as a supported nanoparticle on zeolites [138]. The authors ascribed the observed peak to mononuclear Ag(I) which shifted as the paramagnetic effects of Ag clusters dominated at high loading [139]. Though this is a spin ½ nucleus with a relatively high natural abundance (48%), the gyromagnetic ratio is quite small (-1.25×10^7 rad s^{-1} T^{-1}), leading to poor sensitivity. ^{109}Ag is preferred over ^{107}Ag due to better sensitivity.

It should also be noted that the ^{105}Pd nucleus has been studied in select catalytic Pd complexes, but applications to supported Pd catalysts have been limited by a modest natural abundance (22%), low gyromagnetic ratio (-1.23×10^7 rad s^{-1} T^{-1}), and high quadrupole moment ($I = 5/2$, 66 fm^2) [140]. Recently, a pair of studies have approached the challenge to understand the structure of Pd-containing catalysts in diamagnetic complexes and supported systems. Hooper et al. established the sensitivity of the nucleus to distortions in the material structure and highlighted the sensitivity for NMR to detect such changes in static spectra [141]. They were further able to employ the Knight shift as a sensitive probe of the particle size. Recently, this approach was applied to understand the modification of carbon-supported Pd nanoparticles doped with boron atoms [142]. Short-ranged structural distortions were observed where the presence of interstitial B distorted the lattice to an extent sufficient to broaden the features out of observation. Typical linewidths for these solid materials ranged from 13,000 to 80,000 Hz.

The detection of ^{17}O species is of extensive interest to the advancement of catalyst applications. As the only stable and NMR-active isotope of oxygen, it holds striking importance for a detailed understanding of catalyst systems which very often contain oxygen as either a component of the catalytically active material or as a component of the substrates in the reaction network, just as in energy storage applications. Unfortunately, such observations are not yet routine owing to the significant quadrupolar broadening and low natural abundance (0.0373%). Despite these challenges, it remains a key tool to provide detailed catalyst characterization of oxide materials to the extent that a pair of excellent reviews has covered just this nucleus alone, one focusing on its application to catalysis [143, 144]. Solid powders of metal oxides have been extensively studied which exemplify the sensitivity of oxygen to the bonding metals [145–153]. Due to the low natural abundance, such investigations typically require the use of enriched precursors to identify the local structure of lattice, hydroxyl, and support-metal bridging positions from MQMAS [154]. Enrichment often proceeds via the introduction and incorporation of $H_2{}^{17}O$ or $^{17}O_2$ into the catalyst sample as a replacement for the oxygen already present either through scrambling or redox cycles. Such a strategy has enabled the distinction of oxygen environments on the surface and first few layers of cerium oxide from the bulk species via contrasting chemical shifts [151]. It has also enabled the distinction of unique oxygen sites on zeolite materials such as Si-O-Al, Si-O-Si, and Si-OH-Al in HY or MFI zeolite [147, 155, 156]. Large quadrupole coupling constants and asymmetry parameters manifest themselves for the Si-OH-Al species. Notably, the unique crystallographic positions of framework oxygen and those near Brønsted acids could be resolved with MQMAS NMR with a negative linear correlation between bond angle and chemical shift [157]. In addition to looking at oxygen in the catalyst structure, a number of studies have investigated the adsorption of oxygen-containing compounds onto the material to understand the activation of oxygen or to probe the acid site strength through trimetylphosphine [146, 158]. Given the detailed information such a nucleus provides, techniques to enhance the signal of ^{17}O nuclei are under development. Such technologies as dynamic nuclear polarization (DNP) and double-frequency sweep (DFS) have shown considerable promise in improving the intensity of ^{17}O signals [159].

34.7 Outlook

This brief account of the importance of high-field NMR has described the underlying challenges associated with NMR spectroscopy on quadrupolar, low-γ, and low-natural-abundance nuclei. The enhancements in sensitivity and resolution afforded by a strong magnetic field are critical to the successful detection of several nuclear species. Applications of the technology to the relatively mature high-field ^{27}Al MAS NMR for catalysis were recounted and complemented by those for ^{51}V MAS NMR. Additional insight has also been provided for high-field investigation of energy storage materials and low-sensitivity nuclei. Despite these advances, several nuclei remain relatively insensitive for routine detection (^{17}O, ^{47}Ti, ^{49}Ti, ^{55}Mn, ^{67}Zn, ^{91}Zr, ^{183}W, etc.). While more powerful magnets continue to enter service, the rate of this advancement hinders the unique characterization capabilities NMR offers to a variety of systems. To overcome the resource challenges imposed by the poor sensitivity of these nuclei, a relatively new technique, dynamic nuclear polarization (DNP), should be regarded as an emerging compliment to solid-state NMR. DNP has demonstrated enhancements of up to 400 times the signals which are possible by NMR through the addition of a polarizing agent or by utilizing a radical species native to the sample of interest. It works by transferring polarization from the radical species to the nucleus by microwave irradiation at the electron paramagnetic resonance (EPR) frequency, taking advantage of the much higher gyromagnetic ratio of electrons [160]. This technique enables 2D experiments which are not realistically achievable with MAS NMR by boosting the sensitivity [161, 162]. Illustrated in Fig. 34.20, DNP-NMR has been used to analyze a mixed oxide material of V-Mo-W and was shown to promote the intensity of the vanadium signal by a factor of 50. Since the acquisition time of the experiment scales with the square of the signal-to-noise ratio, the use of

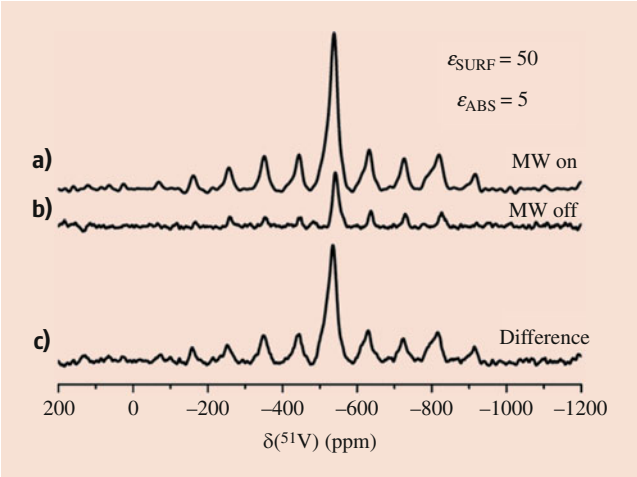

Fig. 34.20 ^{51}V MAS DNP of $V_2Mo_8W_{0.5}O_y$ at a spinning speed of 10 kHz, ns = 30,000, recycle delay 1 s, experimental time 8 h: (**a**) Spectrum measured with microwave (MW on), (**b**) spectrum measured without microwave (MW off) and (**c**) difference spectrum of spectra a and b representing only the surface near ^{51}V. (Reprinted with permission from Thankamony et al. [163]. Copyright 2017 American Chemical Society)

DNP-NMR equated to a time savings of 250 times that of MAS NMR [163]. This emerging technology could render 2D and time-resolved detection of vanadium attainable.

Lapina has provided a summary of DNP NMR's role in characterizing catalytic materials [164]. While applications such as surface-enhanced DNP which provides a two orders of magnitude increase in signal are possible [165, 166], more challenging experiments benefit from combining high magnetic field strength with DNP NMR to dramatically reduce the experimental time for MQMAS and cross polarization experiments [167, 168]. For example, ^{67}Zn, ^{119}Sn, and ^{195}Pt DNP NMR observations have been reported, among others [169–171]. Twice discussed in the context of experimental rigor, it is unsurprising that a number of DNP NMR studies have focused on ^{17}O detection. Using this technology, detection of ^{17}O hydroxyl groups at natural abundance was possible on a silica surface by two-dimensional HETCOR NMR [172]. The quadrupolar Carr-Purcell-Meiboom-Gill (QCPMG) sequence has been combined with DNP NMR to provide unique insight into these silanol groups, providing evidence for the enhanced dehydroxylation propensity of hydrogen-bonded hydroxyls over isolated species [173]. This advancement has enabled further insights into the oxygen environments near Brønsted acid sites. In particular, ^{17}O DNP NMR has been shown to be an accurate probe for determining the O-H bond distance, which has direct implications on the acidity of solid acid catalysts, an important factor in their performance [174]. This work employed windowed-proton-detected local-field QCPMG at natural abundance to determine the O-H bond distance by measuring the dipolar coupling doublet in a series of samples. This was correlated to the pH at the point of zero charge of the surface, correlating longer O-H bond lengths as more acidic in nature [175]. Such a technique was also applied to a Zn/SiO_2 system to demonstrate the increased acidity of hydroxyl groups associated with isolated Zn^{2+} species [176]. Clearly such observations would be nearly impossible at natural abundance without the aid of DNP NMR. The contributions of DNP to ^{17}O observation for catalysis alone highlight the power of this advancement.

Though a promising technology, complications may exist in the deployment of DNP as a spectroscopic technique. In particular, the preparation of materials for DNP NMR is a concern since the added radical species required for the experiment may alter the structure of the catalyst material of interest. Further, such experiments should be performed at low temperatures, which might alter the bonding environment of the nucleus of interest and severely complicate in situ investigations. Such restrictions effectively limit DNP to a quasi ex situ technique at present. Further efforts are required to mitigate these challenges to ensure the sample conditions monitored are representative of the catalyst at relevant conditions. Finally, the equipment necessary to conduct high-field DNP experiments is less accessible than even high-field NMR, severely limiting the ability for DNP to be widely employed. Such technical challenges will hopefully be resolved as DNP-NMR methods mature.

Combining in situ NMR technology with DNP will provide endless routes for advanced catalyst characterization. Indeed, future developments in high-field and/or DNP NMR will drive catalyst research towards the more common implementation of 2D and time-resolved studies of insensitive or time-consuming nuclei such as ^{51}V. Already in our laboratory, smaller in situ rotor designs capable of spinning at rates relevant to high-field ^{27}Al NMR are being employed to monitor the dynamic environments of zeolite materials. Such in situ studies at high field will represent a powerful tool in future investigations. Combining such in situ high-field features with DNP NMR offers possibilities to explore chemical interactions in ways not previously possible.

Acknowledgments

This work was supported by the US Department of Energy, Office of Science, Basic Energy Sciences, Chemical Sciences, Geoscieces, and Bioscieces Division, Catalysis Science program, FWP 47319. Pacific Northwest National Laboratory is a multi-program national laboratory operated by Battelle for the US Department of Energy under Contract DE-AC05-76RL0 1830. The review on energy storage systems was supported by the Joint Center for Energy Storage Research (JCESR), an Energy Innovation Hub funded by the US Department of Energy, Office of Science, Office of Basic Energy Sciences (BES), FWP 63076.

References

1. Research, G.V.: Catalyst market size, share & trends analysis report by product (heterogeneous, homogeneous), by raw material (zeolite, metals), by application (chemical synthesis, environmental), and segment forecasts, 2019–2025. Grand View Res., 250 (2019). https://www.grandviewresearch.com/industry-analysis/inorganic-catalyst-market-report
2. Levitt, M.: Spin Dynamics: Basics of Nuclear Magnetic Resonance, p. 686. Wiley, New York (2001)
3. Andrew, E.R., Bradbury, A., Eades, R.G.: Nuclear magnetic resonance spectra from a crystal rotated at high speed. Nature. **182**(4650), 1659–1659 (1958)
4. Lowe, I.J.: Free induction decays of rotating solids. Phys. Rev. Lett. **2**(7), 285–287 (1959)
5. Maricq, M.M., Waugh, J.S.: NMR in rotating solids. J. Chem. Phys. **70**(7), 3300–3316 (1979)
6. Keeler, J.: Understanding NMR Spectroscopy, 2nd edn. Wiley, Hoboken (2010)
7. Smith, S.A., Palke, W.E., Gerig, J.T.: The Hamiltonians of NMR. Part I. Concepts Magn. Reson. **4**(2), 107–144 (1992)
8. Hu, J.Z., Jaegers, N.R., Hu, M.Y., Mueller, K.T.: In situ and ex situ NMR for battery research. J. Phys. Condens. Mater. **30**(46), 463001 (2018)
9. Bryant, R.G.: The NMR time scale. J. Chem. Educ. **60**(11), 933–935 (1983)
10. Medek, A., Frydman, L.: Multiple-quantum magic-angle spinning NMR: a new technique for probing quadrupolar nuclei in solids. J. Brazil Chem. Soc. **10**(4), 263–277 (1999)

11. Medek, A., Frydman, L.: Quadrupolar and chemical shift tensors characterized by 2D multiple-quantum NMR spectroscopy. J. Magn. Reson. **138**(2), 298–307 (1999)
12. Bornes, C., Sardo, M., Lin, Z., Amelse, J., Fernandes, A., Ribeiro, M.F., Geraldes, C., Rocha, J., Mafra, L.: H-1-P-31 HETCOR NMR elucidates the nature of acid sites in zeolite HZSM-5 probed with trimethylphosphine oxide. Chem. Commun. **55**(84), 12635–12638 (2019)
13. Zheng, A.M., Liu, S.B., Deng, F.: P-31 NMR chemical shifts of phosphorus probes as reliable and practical acidity scales for solid and liquid catalysts. Chem. Rev. **117**(19), 12475–12531 (2017)
14. Jaegers, N.R., Hu, M.Y., Hoyt, D.W., Wang, Y., Hu, J.Z.: Development and application of in situ high-temperature, high-pressure magic angle spinning NMR. In: Webb, G.A. (ed.) Modern Magnetic Resonance, pp. 1–19. Springer International Publishing, Cham (2017)
15. Jaegers, N.R., Mueller, K.T., Wang, Y., Hu, J.Z.: Variable temperature and pressure operando MAS NMR for catalysis science and related materials. Acc. Chem. Res. **53**(3), 611–619 (2020)
16. Jaegers, N.R., Hu, W.D., Wang, Y., Hu, J.Z.: High-temperature and high-pressure in situ magic angle spinning nuclear magnetic resonance spectroscopy. JoVE J. Vis. Exp. **164** (2020). https://doi.org/10.3791/61794
17. Wang, M., Jaegers, N.R., Lee, M.S., Wan, C., Hu, J.Z., Shi, H., Mei, D.H., Burton, S.D., Camaioni, D.M., Gutierrez, O.Y., Glezakou, V.A., Rousseau, R., Wang, Y., Lercher, J.A.: Genesis and stability of hydronium ions in zeolite channels. J. Am. Chem. Soc. **141**(8), 3444–3455 (2019)
18. Dagle, V.L., Winkelman, A.D., Jaegers, N.R., Saavedra-Lopez, J., Hu, J.Z., Engelhard, M.H., Habas, S.E., Akhade, S.A., Kovarik, L., Glezakou, V.A., Rousseau, R., Wang, Y., Dagle, R.A.: Single-step conversion of ethanol to n-butene over ag-ZrO2/SiO2 catalysts. ACS Catal. **10**(18), 10602–10613 (2020)
19. Bryce, D.L., Wasylishen, R.E.: Quadrupolar nuclei in solids: influence of different interactions on spectra. eMagRes. (2011)
20. Massiot, D., Fayon, F., Capron, M., King, I., Le Calve, S., Alonso, B., Durand, J.O., Bujoli, B., Gan, Z.H., Hoatson, G.: Modelling one- and two-dimensional solid-state NMR spectra. Magn. Reson. Chem. **40**(1), 70–76 (2002)
21. Henning, A.: Advanced spectral quantification: parameter handling, nonparametric pattern modeling, and multidimensional fitting. eMagRes. **5**(1), 981–994 (2016)
22. Kemp, T.F., Smith, M.E.: QuadFit – a new cross-platform computer program for simulation of NMR line shapes from solids with distributions of interaction parameters. Solid State Nucl. Magn. Reson. **35**(4), 243–252 (2009)
23. Varian, I.N.S.: VnmrJ Command and Parameter Reference, 2.2C; (2007)
24. van Meerten, S.G.J., Franssen, W.M.J., Kentgens, A.P.M.: ssNake: a cross-platform open-source NMR data processing and fitting application. J. Magn. Reson. **301**, 56–66 (2019)
25. Perras, F.A., Widdifield, C.M., Bryce, D.L.: QUEST-QUadrupolar Exact SofTware: a fast graphical program for the exact simulation of NMR and NQR spectra for quadrupolar nuclei. Solid State Nucl. Magn. Reson. **45-46**, 36–44 (2012)
26. Duer, M.J., Farnan, I.: Quadrupole coupling: its measurement and uses. In: Solid-State NMR Spectroscopy Principles and Applications, pp. 179–215. Wiley, Chichester (2001)
27. Duer, M.J.: Introduction to Solid-State NMR Spectroscopy, p. 368. Wiley-Blackwell, Oxford, England (2005)
28. Haeberlen, U.: High Resolution NMR in Solids Selective Averaging, p. 204. Elsevier, Berlin (1976)
29. Gerstein, B.C., Dybowski, C.R.: Transient Techniques in NMR of Solids: an Introduction to Theory and Practice, p. 320. Academic Press, Orlando (1983)
30. Schmidt-Rohr, K., Spiess, H.W.: Multidimensional Solid-State NMR and Polymers. Academic Press, London (1996)
31. Mackenzie, K.J.D., Smith, M.E.: Multinuclear Solid-State NMR of Inorganic Materials, vol. 6. Pergamon, New York (2002)
32. Man, P.P.: Quadrupole couplins in nuclear magnetic resonance, general. In: Encyclopedia of Analytical Chemistry, pp. 12224–12265. Chichester, Wiley (2002)
33. Forgeron, M.A.M., Bryce, D.L., Wasylishen, R.E., Rosler, R.: A solid-state multinuclear magnetic resonance investigation of hexamethylborazine. J. Phys. Chem. A. **107**(5), 726–735 (2003)
34. Hu, J.Z., Wan, C., Vjunov, A., Wang, M., Zhao, Z.C., Hu, M.Y., Camaioni, D.M., Lercher, J.A.: Al-27 MAS NMR studies of HBEA zeolite at low to high magnetic fields. J. Phys. Chem. C. **121**(23), 12849–12854 (2017)
35. Fyfe, C.A., Bretherton, J.L., Lam, L.Y.: Solid-state NMR detection, characterization, and quantification of the multiple aluminum environments in US-Y catalysts by Al-27 MAS and MQMAS experiments at very high field. J. Am. Chem. Soc. **123**(22), 5285–5291 (2001)
36. Schwalbe, H.: New 1.2 GHz NMR spectrometers – new horizons? Angew. Chem. Int. Edit. **56**(35), 10252–10253 (2017)
37. Lapina, O.B., Khabibulin, D.F., Terskikh, V.V.: Multinuclear NMR study of silica fiberglass modified with zirconia. Solid State Nucl. Magn. Reson. **39**(3–4), 47–57 (2011)
38. Gan, Z.H., Gor'kov, P., Cross, T.A., Samoson, A., Massiot, D.: Seeking higher resolution and sensitivity for NMR of quadrupolar nuclei at ultrahigh magnetic fields. J. Am. Chem. Soc. **124**(20), 5634–5635 (2002)
39. Lapina, O.B., Terskikh, V.V.: Quadrupolar metal NMR of oxide materials including catalysts. eMagRes. (2011)
40. Wasylishen, R.E., Ashbrook, S.E., Wimperis, S.: NMR of Quadrupolar Nuclei in Solid Materials, p. 550. Wiley, Chichester (2012)
41. Vega, A.J.: Quadrupolar nuclei in solids. eMagRes. (2010)
42. Quinn, C.M., Wang, M., Polenova, T.: NMR of Macromolecular Assemblies and Machines at 1 GHz and Beyond: New Transformative Opportunities for Molecular Structural Biology, vol. 1688. Humana Press, New York (2018)
43. Ballesteros, R., Fajardo, M., Sierra, I., Force, C., del Hierro, I.: Solid-state Ti-49/47 NMR of titanium-based MCM-41 hybrid materials. Langmuir. **25**(21), 12706–12712 (2009)
44. Lucier, B.E.G., Huang, Y.N.: A review of Zr-91 solid-state nuclear magnetic resonance spectroscopy. Annu. Rep. NMR Spectrosc. **84**, 233–289 (2015)
45. Ashbrook, S.E., Smith, M.E.: Solid state O-17 NMR – an introduction to the background principles and applications to inorganic materials. Chem. Soc. Rev. **35**(8), 718–735 (2006)
46. Haouas, M., Taulelle, F., Martineau, C.: Recent advances in application of Al-27 NMR spectroscopy to materials science. Prog. Nucl. Magn. Reson. Spectrosc. **94-95**, 11–36 (2016)
47. Benesi, A.J.: A Primer of NMR Theory with Calculations in Mathematica, p. 237. Wiley, Hoboken (2015)
48. Weller, M.T., Brenchley, M.E., Apperley, D.C., Davies, N.A.: Correlations between Al-27 magic-angle-spinning nuclear-magnetic-resonance spectra and the coordination geometry of framework aluminates. Solid State Nucl. Magn. Reson. **3**(2), 103–106 (1994)
49. Kohn, S.C., Henderson, C.M.B., Dupree, R.: Si-Al ordering in leucite group minerals and ion-exchanged analogues: an MAS NMR study. Am. Mineral. **82**(11–12), 1133–1140 (1997)
50. Phillips, B.L., Kirkpatrick, R.J.: Short-range Si-Al order in leucite and analcime – determination of the configurational entropy from Al-27 and variable-temperature Si-29 NMR-spectroscopy of leucite, its Cs-exchanged and Rb-exchanged derivatives, and analcime. Am. Mineral. **79**(11–12), 1025–1031 (1994)

51. Phillips, B.L., Kirkpatrick, R.J., Putnis, A.: Si, Al ordering in leucite by high-resolution Al-27 MAS NMR-spectroscopy. Phys. Chem. Miner. **16**(6), 591–598 (1989)
52. Hovis, G.L., Spearing, D.R., Stebbins, J.F., Roux, J., Clare, A.: X-ray-powder diffraction and Na-23, Al-27, and Si-29 mas-NMR investigation of nepheline-kalsilite crystalline solutions. Am. Mineral. **77**(1–2), 19–29 (1992)
53. Lippmaa, E., Samoson, A., Magi, M.: High-resolution Al-27 NMR of aluminosilicates. J. Am. Chem. Soc. **108**(8), 1730–1735 (1986)
54. Smith, S.J., Amin, S., Woodfield, B.F., Boerio-Goates, J., Campbell, B.J.: Phase progression of gamma-Al2O3 nanoparticles synthesized in a solvent-deficient environment. Inorg. Chem. **52**(8), 4411–4423 (2013)
55. Perander, L.M., Zujovic, Z.D., Groutso, T., Hyland, M.M., Smith, M.E., O'Dell, L.A., Metson, J.B.: Characterization of metallurgical-grade aluminas and their precursors by (27)AI NMR and XRD1. Can. J. Chem. **85**(10), 889–897 (2007)
56. Duvel, A., Romanova, E., Sharifi, M., Freude, D., Wark, M., Heitjans, P., Wilkening, M.: Mechanically induced phase transformation of gamma-Al2O3 into alpha-Al2O3. Access to structurally disordered gamma-Al2O3 with a controllable amount of penta-coordinated Al sites. J. Phys. Chem. C. **115**(46), 22770–22780 (2011)
57. Hu, J.Z., Zhang, X., Jaegers, N.R., Wan, C., Graham, T.R., Hu, M., Pearce, C.I., Felmy, A.R., Clark, S.B., Rosso, K.M.: Transitions in Al coordination during gibbsite crystallization using high-field Al-27 and Na-23 MAS NMR spectroscopy. J. Phys. Chem. C. **121**(49), 27555–27562 (2017)
58. Zhang, X., Huestis, P.L., Pearce, C.I., Hu, J.Z., Page, K., Anovitz, L.M., Aleksandrov, A.B., Prange, M.P., Kerisit, S., Bowden, M.E., Cui, W., Wang, Z., Jaegers, N.R., Graham, T.R., Dembowski, M., Wang, H.-W., Liu, J., N'Diaye, A.T., Bleuel, M., Mildner, D.F.R., Orlando, T.M., Kimmel, G.A., La Verne, J.A., Clark, S.B., Rosso, K.M.: Boehmite and gibbsite nanoplates for the synthesis of advanced alumina products. ACS Appl. Nano Mater. **1**(12), 7115–7128 (2018)
59. Graham, T.R., Dembowski, M., Martinez-Baez, E., Zhang, X., Jaegers, N.R., Hu, J.Z., Gruszkiewicz, M.S., Wang, H.W., Stack, A.G., Bowden, M.E., Delegard, C.H., Schenter, G.K., Clark, A.E., Clark, S.B., Felmy, A.R., Rosso, K.M., Pearce, C.I.: In situ Al-27 NMR spectroscopy of aluminate in sodium hydroxide solutions above and below saturation with respect to gibbsite. Inorg. Chem. **57**(19), 11864–11873 (2018)
60. Graham, T.R., Hu, J.Z., Zhang, X., Dembowski, M., Jaegers, N.R., Wan, C., Bowden, M., Lipton, A.S., Felmy, A.R., Clark, S.B., Rosso, K.M., Pearce, C.I.: Unraveling gibbsite transformation pathways into LiAl-LDH in concentrated lithium hydroxide. Inorg. Chem. **58**(18), 12385–12394 (2019)
61. Xu, S.C., Jaegers, N.R., Hu, W.D., Kwak, J.H., Bao, X.H., Sun, J.M., Wang, Y., Hu, J.Z.: High-field one-dimensional and two-dimensional Al-27 magic-angle spinning nuclear magnetic resonance study of theta-, delta-, and gamma-Al2O3 dominated aluminum oxides: toward understanding the Al sites in gamma-Al2O3. ACS Omega. **6**(5), 4090–4099 (2021)
62. Kovarik, L., Bowden, M., Andersen, A., Jaegers, N.R., Washton, N., Szanyi, J.: Quantification of high-temperature transition Al2O3 and their phase transformations. Angew. Chem. Int. Edit. **59**(48), 21719–21727 (2020)
63. Hu, J.Z., Xu, S.C., Kwak, J.H., Hu, M.Y., Wan, C., Zhao, Z.C., Szanyi, J., Bao, X.H., Han, X.W., Wang, Y., Peden, C.H.F.: High field Al-27 MAS NMR and TPD studies of active sites in ethanol dehydration using thermally treated transitional aluminas as catalysts. J. Catal. **336**, 85–93 (2016)
64. Kwak, J.H., Hu, J.Z., Mei, D., Yi, C.W., Kim, D.H., Peden, C.H.F., Allard, L.F., Szanyi, J.: Coordinatively unsaturated Al3+ centers as binding sites for active catalyst phases of platinum on gamma-Al2O3. Science. **325**(5948), 1670–1673 (2009)
65. Wan, C., Hu, M.Y., Jaegers, N.R., Shi, D.C., Wang, H.M., Gao, F., Qin, Z.H., Wang, Y., Hui, J.Z.: Investigating the surface structure of gamma-Al2O3 supported WOx catalysts by high field Al-27 MAS NMR and electronic structure calculations. J. Phys. Chem. C. **120**(40), 23093–23103 (2016)
66. Khivantsev, K., Jaegers, N.R., Kovarik, L., Prodinger, S., Derewinski, M.A., Wang, Y., Gao, F., Szanyi, J.: Palladium/Beta zeolite passive NOx adsorbers (PNA): clarification of PNA chemistry and the effects of CO and zeolite crystallite size on PNA performance. Appl. Catal. A Gen. **569**, 141–148 (2019)
67. Khivantsev, K., Jaegers, N.R., Kovarik, L., Hu, J.Z., Gao, F., Wang, Y., Szanyi, J.: Palladium/zeolite low temperature passive NOx adsorbers (PNA): structure-adsorption property relationships for hydrothermally aged PNA materials. Emiss. Control Sci. Technol. **6**, 126–138 (2019)
68. Jaegers, N.R., Khivantsev, K., Kovarik, L., Klas, D.W., Hu, J.Z., Wang, Y., Szanyi, J.: Catalytic activation of ethylene C–H bonds on uniform d8 Ir(i) and Ni(ii) cations in zeolites: toward molecular level understanding of ethylene polymerization on heterogeneous catalysts. Cat. Sci. Technol. **9**(23), 6570–6576 (2019)
69. Mali, G., Taulelle, F.: Detecting proximities between quadrupolar nuclei by double-quantum NMR. Chem. Commun. **7**, 868–869 (2004)
70. Malicki, N., Mali, G., Quoineaud, A.A., Bourges, P., Simon, L.J., Thibault-Starzyk, F., Fernandez, C.: Aluminium triplets in dealuminated zeolites detected by Al-27 NMR correlation spectroscopy. Micropor. Mesopor. Mater. **129**(1–2), 100–105 (2010)
71. Yu, Z.W., Zheng, A.M., Wang, Q.A., Chen, L., Xu, J., Amoureux, J.P., Deng, F.: Insights into the dealumination of zeolite HY revealed by sensitivity-enhanced Al-27 DQ-MAS NMR spectroscopy at high field. Angew. Chem. Int. Edit. **49**(46), 8657–8661 (2010)
72. Altwasser, S., Jiao, J., Steuernagel, S., Weitkamp, J., Hunger, M.: Elucidating the dealumination mechanism of zeolite H-Y by solid-state NMR spectroscopy. Recent Adv. Sci. Technol. Zeolites Relat. Mater. Pts A-C. **154**, 3098–3105 (2004)
73. Weeks, M.E.: The discovery of the elements. VII. Columbium, tantalum, and vanadium. J. Chem. Educ. **9**(5), 863 (1932)
74. Cook, E.: Peregrine Phillips, the inventor of the contact process for sulphuric acid. Nature. **117**, 419–421 (1926)
75. Wachs, I.E.: The generality of surface vanadium oxide phases in mixed oxide catalysts. Appl. Catal. A Gen. **391**(1–2), 36–42 (2011)
76. Sattler, J.J.H.B., Ruiz-Martinez, J., Santillan-Jimenez, E., Weckhuysen, B.M.: Catalytic dehydrogenation of light alkanes on metals and metal oxides. Chem. Rev. **114**(20), 10613–10653 (2014)
77. Wachs, I.E., Deo, G., Weckhuysen, B.M., Andreini, A., Vuurman, M.A., de Boer, M., Amiridis, M.D.: Selective catalytic reduction of NO with NH3 over supported vanadia catalysts. J. Catal. **161**(1), 211–221 (1996)
78. Wachs, I.E., Jehng, J.-M., Deo, G., Weckhuysen, B.M., Guliants, V.V., Benziger, J.B., Sundaresan, S.: Fundamental studies of butane oxidation over model-supported vanadium oxide catalysts: molecular structure-reactivity relationships. J. Catal. **170**(1), 75–88 (1997)
79. Wachs, I.E.: Catalysis science of supported vanadium oxide catalysts. Dalton Trans. **42**(33), 11762–11769 (2013)
80. Langeslay, R.R., Kaphan, D.M., Marshall, C.L., Stair, P.C., Sattelberger, A.P., Delferro, M.: Catalytic applications of vanadium: a mechanistic perspective. Chem. Rev. **119**(4), 2128–2191 (2019)
81. Lv, H.J., Song, J., Geletii, Y.V., Vickers, J.W., Sumliner, J.M., Musaev, D.G., Kogerler, P., Zhuk, P.F., Bacsa, J., Zhu, G.B., Hill, C.L.: An exceptionally fast homogeneous carbon-free cobalt-based

water oxidation catalyst. J. Am. Chem. Soc. **136**(26), 9268–9271 (2014)
82. Maurya, M.R., Arya, A., Kumar, A., Kuznetsov, M.L., Avecilla, F., Pessoa, J.C.: Polymer-bound oxidovanadium(IV) and dioxidovanadium(V) complexes as catalysts for the oxidative desulfurization of model fuel diesel. Inorg. Chem. **49**(14), 6586–6600 (2010)
83. Gupta, R., Hou, G.J., Renirie, R., Wever, R., Polenova, T.: V-51 NMR crystallography of vanadium chloroperoxidase and its directed evolution P395D/L241V/T343A mutant: protonation environments of the active site. J. Am. Chem. Soc. **137**(16), 5618–5628 (2015)
84. Bleaney, B., Gregg, J.F., Wells, M.R.: The ratio of the nuclear electric quadrupole-moments of V-50 and V-51 in Smvo4. J. Phys. C Solid State. **15**(11), L349–L352 (1982)
85. Lapina, O.B., Mastikhin, V.M., Shubin, A.A., Krasilnikov, V.N., Zamaraev, K.I.: 51V solid state NMR studies of vanadia based catalysts. Prog. Nucl. Magn. Reson. Spectrosc. **24**(6), 457–525 (1992)
86. Lapina, O.B., Khabibulin, D.F., Shubin, A.A., Terskikh, V.V.: Practical aspects of V-51 and Nb-93 solid-state NMR spectroscopy and applications to oxide materials. Prog. Nucl. Magn. Reson. Spectrosc. **53**(3), 128–191 (2008)
87. Pourpoint, F., Trebosc, J., Bonhomme, C., Durupthy, O., Steunou, N., Lafon, O., Amoureux, J.P.: Quantitative analysis of the proximities of OH ligands and vanadium sites in a polyoxovanadate cluster using frequency-selective H-1-V-51 solid-state NMR spectroscopy. J. Phys. Chem. C. **118**(32), 18580–18588 (2014)
88. Eckert, H., Wachs, I.E.: Solid-state vanadium-51 NMR structural studies on supported vanadium(V) oxide catalysts: vanadium oxide surface layers on alumina and titania supports. J. Phys. Chem. **93**, 6796 (1989)
89. Luca, V., Thomson, S., Howe, R.F.: Spectroscopic investigation of vanadium speciation in vanadium-doped nanocrystalline anatase. J. Chem. Soc. Faraday T. **93**(12), 2195–2202 (1997)
90. Kalinkin, P., Kovalenko, O., Lapina, O., Khabibulin, D., Kundo, N.: Kinetic peculiarities in the low-temperature oxidation of H2S over vanadium catalysts. J. Mol. Catal. A Chem. **178**(1–2), 173–180 (2002)
91. Borovkov, V.Y., Mikheeva, E.P., Zhidomirov, G.M., Lapina, O.B.: Theoretical and experimental studies of the nature of the catalytic activity of VOx/TiO2 systems. Kinet. Catal. **44**(5), 710–717 (2003)
92. Hu, J.Z., Xu, S., Li, W.-Z., Hu, M.Y., Deng, X., Dixon, D.A., Vasiliu, M., Craciun, R., Wang, Y., Bao, X., Peden, C.H.F.: Investigation of the structure and active sites of TiO2 nanorod supported VOx catalysts by high-field and fast-spinning 51V MAS NMR. ACS Catal. **5**(7), 3945–3952 (2015)
93. Jaegers, N.R., Lai, J.K., He, Y., Walter, E., Dixon, D.A., Vasiliu, M., Chen, Y., Wang, C.M., Hu, M.Y., Mueller, K.T., Wachs, I.E., Wang, Y., Hu, J.Z.: Mechanism by which tungsten oxide promotes the activity of supported V2O5/TiO2 catalysts for NOX abatement: structural effects revealed by V-51 MAS NMR spectroscopy. Angew. Chem. Int. Edit. **131**, 12739–12746 (2019)
94. Kwak, J.H., Herrera, J.E., Hu, J.Z., Wang, Y., Peden, C.H.F.: A new class of highly dispersed VOx catalysts on mesoporous silica: synthesis, characterization, and catalytic activity in the partial oxidation of ethanol. Appl. Catal. A Gen. **300**(2), 109–119 (2006)
95. Bineesh, K.V., Kim, M.I., Lee, G.H., Selvaraj, M., Park, D.W.: Catalytic performance of vanadia-doped alumina-pillared clay for selective oxidation of H2S. Appl. Clay Sci. **74**, 127–134 (2013)
96. Lapina, O.B., Shubin, A.A., Khabibulin, D.F., Terskikh, V.V., Bodart, P.R., Amoureux, J.P.: Solid-state V-51 NMR for characterization of vanadium-containing systems. Catal. Today. **78**(1–4), 91–104 (2003)
97. Das, N., Eckert, H., Hu, H., Wachs, I.E., Walzer, J.F., Feher, F.J.: Bonding states of surface vanadium(V) oxide phases on silica: structural characterization by vanadium-51 NMR and Raman spectroscopy. J. Phys. Chem. **97**(31), 8240–8243 (1993)
98. Schimmoeller, B., Jiang, Y., Pratsinis, S.E., Baiker, A.: Structure of flame-made vanadia/silica and catalytic behavior in the oxidative dehydrogenation of propane. J. Catal. **274**(1), 64–75 (2010)
99. Grant, J.T., Carrero, C.A., Love, A.M., Verel, R., Hermans, I.: Enhanced two-dimensional dispersion of group V metal oxides on silica. ACS Catal. **5**(10), 5787–5793 (2015)
100. Barman, S., Maity, N., Bhatte, K., Ould-Chikh, S., Dachwald, O., Haeßner, C., Saih, Y., Abou-Hamad, E., Llorens, I., Hazemann, J.-L., Köhler, K., D'Elia, V., Basset, J.-M.: Single-site VOx moieties generated on silica by surface organometallic chemistry: a way to enhance the catalytic activity in the oxidative dehydrogenation of propane. ACS Catal. **6**(9), 5908–5921 (2016)
101. Jaegers, N.R., Wan, C., Hu, M.Y., Vasiliu, M., Dixon, D.A., Walter, E., Wachs, I.E., Wang, Y., Hu, J.Z.: Investigation of silica-supported vanadium oxide catalysts by high-field 51V magic-angle spinning NMR. J. Phys. Chem. C. **121**(11), 6246–6254 (2017)
102. de Oliveira Jr, M., Seeburg, D., Weiss, J., Wohlrab, S., Buntkowsky, G., Bentrup, U., Gutmann, T.: Structural characterization of vanadium environments in MCM-41 molecular sieve catalysts by solid state 51V NMR. Cat. Sci. Technol. **9**, 6180 (2019)
103. Nielsen, U.G., Boisen, A., Brorson, M., Jacobsen, C.J.H., Jakobsen, H.J., Skibsted, J.: Aluminum orthovanadate (AlVO4): synthesis and characterization by Al-27 and V-51 MAS and MQMAS NMR spectroscopy. Inorg. Chem. **41**(24), 6432–6439 (2002)
104. Lapina, O.B., Khabibulin, D.F., Shubin, A.A., Bondareva, V.M.: V-51 and P-31 NMR studies of VOx/TiO2 catalysts modified by phosphorous. J. Mol. Catal. A Chem. **162**(1–2), 381–390 (2000)
105. Hu, J.Z., Kwak, J.H., Yang, Z.G., Osborn, W., Markmaitree, T., Shaw, L.L.: Investigation of mechanical activation on Li-N-H systems using Li-6 magic angle spinning nuclear magnetic resonance at ultra-high field. J. Power Sources. **182**(1), 278–283 (2008)
106. Wan, C., Xu, S., Hu, M.Y., Cao, R., Qian, J., Qin, Z., Liu, J., Mueller, K.T., Zhang, J.G., Hu, J.Z.: Multinuclear NMR study of the solid electrolyte interface formed in lithium metal batteries. ACS Appl. Mater. Interfaces. **9**(17), 14741–14748 (2017)
107. Hung, I., Zhou, L.N., Pourpoint, F., Grey, C.P., Gan, Z.H.: Isotropic high field NMR spectra of Li-ion battery materials with anisotropy >1 MHz. J. Am. Chem. Soc. **134**(4), 1898–1901 (2012)
108. Meyer, B.M., Leifer, N., Sakamoto, S., Greenbaum, S.G., Grey, C.P.: High field multinuclear NMR investigation of the SEI layer in lithium rechargeable batteries. Electrochem. Solid-State Lett. **8**(3), A145–A148 (2005)
109. Wan, C., Hu, M.Y., Borodin, O., Qian, J., Qin, Z., Zhang, J.-G., Hu, J.Z.: Natural abundance 17 O, 6 Li NMR and molecular modeling studies of the solvation structures of lithium bis(fluorosulfonyl) imide/1,2-dimethoxyethane liquid electrolytes. J. Power Sources. **307**, 231–243 (2016)
110. Deng, X., Hu, M.Y., Wei, X., Wang, W., Chen, Z., Liu, J., Hu, J.Z.: Natural abundance 17 O nuclear magnetic resonance and computational modeling studies of lithium based liquid electrolytes. J. Power Sources. **285**, 146–155 (2015)
111. Leskes, M., Moore, A.J., Goward, G.R., Grey, C.P.: Monitoring the electrochemical processes in the lithium-air battery by solid state NMR spectroscopy. J. Phys. Chem. C. **117**(51), 26929–26939 (2013)
112. Chen, Y., Jaegers, N.R., Han, K.S., Wang, H., Young, R.P., Agarwal, G., Lipton, A.S., Assary, R.S., Washton, N.M., Hu, J.Z., Mueller, K.T., Murugesan, V.: Probing conformational evolution and associated dynamics of Mg(N(SO2CF3)(2))(2)center dot dimethoxyethane adduct using solid-state F-19 and H-1 NMR. J. Phys. Chem. C. **124**(9), 4999–5008 (2020)

113. Chen, Y., Jaegers, N.R., Wang, H., Han, K.S., Hu, J.Z., Mueller, K.T., Murugesan, V.: Role of solvent rearrangement on Mg2+ solvation structures in dimethoxyethane solutions using multimodal NMR analysis. J. Phys. Chem. Lett. **11**(15), 6443–6449 (2020)
114. Han, K.S., Hahn, N.T., Zavadil, K.R., Jaegers, N.R., Chen, Y., Hu, J.Z., Murugesan, V., Mueller, K.T.: Factors influencing preferential anion interactions during solvation of multivalent cations in ethereal solvents. J. Phys. Chem. C. **125**(11), 6005–6012 (2021)
115. Lucier, B.E.G., Huang, Y.N.: Reviewing Ti-47/49 solid-state NMR spectroscopy: from alloys and simple compounds to catalysts and porous materials. Annu. Rep. NMR Spectrosc. **88**, 1–78 (2016)
116. de Lacaillerie, J.B.D., Barberon, F., Romanenko, K.V., Lapina, O.B., Le Polles, L., Gautier, R., Gan, Z.H.: Mo-95 magic angle spinning NMR at high field: improved measurements and structural analysis of the quadrupole interaction in monomolybdates and isopolymolybdates. J. Phys. Chem. B. **109**(29), 14033–14042 (2005)
117. Sutrisno, A., Liu, L., Dong, J.X., Huang, Y.N.: Solid-state Zr-91 NMR characterization of layered and three-dimensional framework zirconium phosphates. J. Phys. Chem. C. **116**(32), 17070–17081 (2012)
118. Freitas, J.C.C., Smith, M.E.: Recent advances in solid-state Mg-25 NMR spectroscopy. Annu. Rep. NMR Spectrosc. **75**, 25–114 (2012)
119. Lucier, B.E.G., Huang, Y.: Chapter five – a review of 91Zr solid-state nuclear magnetic resonance spectroscopy. In: Webb, G.A. (ed.) Annual Reports on NMR Spectroscopy, vol. 84, pp. 233–289. Academic Press, London (2015)
120. Dupree, R., Smith, M.E.: Solid-state magnesium-25 NMR-spectroscopy. J. Chem. Soc. Chem. Comm. **22**, 1483–1485 (1988)
121. Fiske, P.S., Stebbins, J.F.: The structural of Mg in silicate liquids – a high-temperature Mg-25, Na-23, and Si-29 NMR-study. Am. Mineral. **79**(9–10), 848–861 (1994)
122. Mackenzie, K.J.D., Meinhold, R.H.: Mg-25 nuclear-magnetic-resonance spectroscopy of minerals and related inorganics – a survey study. Am. Mineral. **79**(3–4), 250–260 (1994)
123. Blaakmeer, E.S., Antinucci, G., Busico, V., van Eck, E.R.H., Kentgens, A.P.M.: Solid-state NMR investigations of MgCl2 catalyst support. J. Phys. Chem. C. **120**(11), 6063–6074 (2016)
124. McCarty, R.J., Stebbins, J.F.: Transition metal dopant cation distributions in MgO and CaO: new inferences from paramagnetically shifted resonances in O-17, Mg-25, and Ca-43 NMR spectra. J. Phys. Chem. C. **120**(20), 11111–11120 (2016)
125. Wagner, G.W., Itin, B.: Comment on "Al-27, Ti-47,Ti-49, P-31, and C-13 MAS NMR study of VX, GD, and HD reactions with nanosize Al2O3, conventional Al2O3 and TiO2, and aluminum and titanium metal". J. Phys. Chem. C. **112**(26), 9962–9962 (2008)
126. He, P., Lucier, B.E.G., Terskikh, V.V., Shi, Q., Dong, J.X., Chu, Y.Y., Zheng, A.M., Sutrisno, A., Huang, Y.N.: Spies within metal-organic frameworks: investigating metal centers using solid-state NMR. J. Phys. Chem. C. **118**(41), 23728–23744 (2014)
127. Zhu, J.F., Trefiak, N., Woo, T.K., Huang, Y.N.: A Ti-47/49 solid-state NMR study of layered titanium phosphates at ultrahigh magnetic field. J. Phys. Chem. C. **113**(23), 10029–10037 (2009)
128. Xu, J., Lucier, B.E.G., Lin, Z., Sutrisno, A., Terskikh, V.V., Huang, Y.N.: New insights into the short-range structures of microporous titanosilicates as revealed by Ti-47/49, Na-23, K-39, and Si-29 solid-state NMR spectroscopy. J. Phys. Chem. C. **118**(47), 27353–27365 (2014)
129. Sutrisno, A., Terskikh, V.V., Shi, Q., Song, Z.W., Dong, J.X., Ding, S.Y., Wang, W., Provost, B.R., Daff, T.D., Woo, T.K., Huang, Y.N.: Characterization of Zn-containing metal-organic frameworks by solid-state 67Zn NMR spectroscopy and computational modeling. Chem. Eur. J. **18**(39), 12251–12259 (2012)
130. Huang, Y.N., Sutrisno, A.: Recent advances in solid-state Zn-67 NMR studies: from nanoparticles to biological systems. Annu. Rep. NMR Spectrosc. **81**, 1–46 (2014)
131. Knight, C.T.G., Turner, G.L., Kirkpatrick, R.J., Oldfield, E.: Solid-state W-183 nuclear-magnetic-resonance spectroscopy. J. Am. Chem. Soc. **108**(23), 7426–7427 (1986)
132. Haouas, M., Trebosc, J., Roch-Marchal, C., Cadot, E., Taulelle, F., Martineau-Corcos, C.: High-field Mo-95 and W-183 static and MAS NMR study of polyoxometalates. Magn. Reson. Chem. **55**(10), 902–908 (2017)
133. Hu, J.Z., Kwak, J.H., Wang, Y., Peden, C.H.F., Zheng, H., Ma, D., Bao, X.: Studies of the active sites for methane dehydroaromatization using ultrahigh-field solid-state Mo-95 NMR spectroscopy. J. Phys. Chem. C. **113**(7), 2936–2942 (2009)
134. Zheng, H., Ma, D., Bao, X.H., Hu, J.Z., Kwak, J.H., Wang, Y., Peden, C.H.F.: Direct observation of the active center for methane dehydroaromatization using an ultrahigh field Mo-95 NMR spectroscopy. J. Am. Chem. Soc. **130**(12), 3722–+ (2008)
135. Looser, H., Brinkmann, D.: Ag-109 chemical-shifts in some solid compounds. J. Magn. Reson. **64**(1), 76–80 (1985)
136. Merwin, L.H., Sebald, A.: The 1st examples of Ag-109 Cp mas spectroscopy. J. Magn. Reson. **97**(3), 628–631 (1992)
137. Dugar, S., Izarova, N.V., Mal, S.S., Fu, R.Q., Joo, H.C., Lee, U., Dalal, N.S., Pope, M.T., Jameson, G.B., Kortz, U.: Characterization of Pt-IV-containing polyoxonietatates by high-resolution solid-state Pt-195 and V-51 NMR spectroscopy. New J. Chem. **40**(2), 923–927 (2016)
138. Pavlovskaya, G.E., Horton-Garcia, C.F., Dybowski, C., Corbin, D.R., Meersmann, T.: Metallic clusters and color changes in silver-exchanged zeolites: Ag-109 solid state NMR and optical studies. J. Phys. Chem. B. **108**(5), 1584–1589 (2004)
139. Popovych, N., Kyriienko, P., Soloviev, S., Baran, R., Millot, Y., Dzwigaj, S.: Identification of the silver state in the framework of Ag-containing zeolite by XRD, FTIR, photoluminescence, Ag-109 NMR, EPR, DR UV-vis, TEM and XPS investigations. Phys. Chem. Chem. Phys. **18**(42), 29458–29465 (2016)
140. Hooper, T.J.N.: Solid State Nuclear Magnetic Resonance on Quadrupolar Nucleiin Disordered Catalysis Based Materials. University of Warwick, Warwick (2017)
141. Hooper, T.J.N., Partridge, T.A., Rees, G.J., Keeble, D.S., Powell, N.A., Smith, M.E., Mikheenko, I.P., Macaskie, L.E., Bishop, P.T., Hanna, J.V.: Direct solid state NMR observation of the Pd-105 nucleus in inorganic compounds and palladium metal systems. Phys. Chem. Chem. Phys. **20**(41), 26734–26743 (2018)
142. Chen, T., Ellis, I., Hooper, T., Liberti, E., Ye, L., Lo, T.W.B., O'Leary, C., Sheader, A.A., Martinez, G.T., Jones, L., Ho, P.-L., Zhao, P., Cookson, J., Bishop, P.T., Chater, P.A., Hanna, J.V., Nellist, P.D., Tsang, S.C.E.: Interstitial boron atoms in palladium lattice of industrial type of nano-catalyst: properties and structural modifications. J. Am. Chem. Soc. **141**, 19616 (2019)
143. Shen, L., Peng, L.M.: O-17 solid-state NMR studies of oxygen-containing catalysts. Chin. J. Catal. **36**(9), 1494–1504 (2015)
144. Ashbrook, S.E., Smith, M.E.: Oxygen-17 NMR of inorganic materials. eMagRes. (2011)
145. He, P., Xu, J., Terskikh, V.V., Sutrisno, A., Nie, H.Y., Huang, Y.N.: Identification of nonequivalent framework oxygen species in metal-organic frameworks by O-17 solid-state NMR. J. Phys. Chem. C. **117**(33), 16953–16960 (2013)
146. Huo, H., Peng, L.M., Gan, Z.H., Grey, C.P.: Solid-state MAS NMR studies of Bronsted acid sites in zeolite H-Mordenite. J. Am. Chem. Soc. **134**(23), 9708–9720 (2012)

147. Peng, L., Huo, H., Liu, Y., Grey, C.P.: O-17 magic angle spinning NMR studies of Bronsted acid sites in zeolites HY and HZSM-5. J. Am. Chem. Soc. **129**(2), 335–346 (2007)
148. Freude, D., Loeser, T., Michel, D., Pingel, U., Prochnow, D.: O-17 NMR studies of low silicate zeolites. Solid State Nucl. Magn. Reson. **20**(1–2), 46–60 (2001)
149. Gervais, C., Babonneau, F., Smith, M.E.: Detection, quantification, and magnetic field dependence of solid-state O-17 NMR of X-O-Y (X,Y = Si,Ti) linkages: implications for characterizing amorphous titania-silica-based materials. J. Phys. Chem. B. **105**(10), 1971–1977 (2001)
150. Gunawidjaja, P.N., Holland, M.A., Mountjoy, G., Pickup, D.M., Newport, R.J., Smith, M.E.: The effects of different heat treatment and atmospheres on the NMR signal and structure of TiO2-ZrO2-SiO2 sol-gel materials. Solid State Nucl. Magn. Reson. **23**(1–2), 88–106 (2003)
151. Wang, M., Wu, X.P., Zheng, S.J., Zhao, L., Li, L., Shen, L., Gao, Y.X., Xue, N.H., Guo, X.F., Huang, W.X., Gan, Z.H., Blanc, F., Yu, Z.W., Ke, X.K., Ding, W.P., Gong, X.Q., Grey, C.P., Peng, L.M.: Identification of different oxygen species in oxide nanostructures with O-17 solid-state NMR spectroscopy. Sci. Adv. **1**(1), e1400133 (2015)
152. Klug, C.A., Kroeker, S., Aguiar, P.M., Zhou, M., Stec, D.F., Wachs, I.E.: Insights into oxygen exchange between gaseous O-2 and supported vanadium oxide catalysts via O-17 NMR. Chem. Mater. **21**(18), 4127–4134 (2009)
153. Pimentel, H.R.X., Aguiar, D.L.M., San Gil, R.A.S., Souza, E.F., Ferreira, A.R., Leitao, A.A., Alencastro, R.B., Menezes, S.M.C., Chiaro, S.S.X.: O-17 MAS NMR and first principles calculations of ZrO2 polymorphs. Chem. Phys. Lett. **555**, 96–100 (2013)
154. Merle, N., Trebosc, J., Baudouin, A., Del Rosal, I., Maron, L., Szeto, K., Genelot, M., Mortreux, A., Taoufik, M., Delevoye, L., Gauvin, R.M.: O-17 NMR gives unprecedented insights into the structure of supported catalysts and their interaction with the silica carrier. J. Am. Chem. Soc. **134**(22), 9263–9275 (2012)
155. Peng, L.M., Liu, Y., Kim, N.J., Readman, J.E., Grey, C.P.: Detection of Bronsted acid sites in zeolite HY with high-field O-17-MAS-NMR techniques. Nat. Mater. **4**(3), 216–219 (2005)
156. Huo, H., Peng, L., Grey, C.P.: Measuring Bronsted acid site O-H distances in zeolites HY and HZSM-5 with low-temperature O-17-H-1 double resonance MAS NMR spectroscopy. J. Phys. Chem. C. **115**(5), 2030–2037 (2011)
157. Peng, L., Huo, H., Gan, Z., Grey, C.P.: O-17 MQMAS NMR studies of zeolite HY. Micropor. Mesopor. Mater. **109**(1–3), 156–162 (2008)
158. Wang, X.F., Han, X.W., Huang, Y.N., Sun, J.M., Xu, S.C., Bao, X.H.: O-17 solid-state NMR study on the size dependence of oxygen activation over silver catalysts. J. Phys. Chem. C. **116**(49), 25846–25851 (2012)
159. Grekov, D., Bouhoute, Y., Del Rosal, I., Maron, L., Taoufik, M., Gauvin, R.M., Delevoye, L.: O-17 MAS NMR studies of oxo-based olefin metathesis catalysts: a critical assessment of signal enhancement methods. Phys. Chem. Chem. Phys. **18**(40), 28157–28163 (2016)
160. Can, T.V., Ni, Q.Z., Griffin, R.G.: Mechanisms of dynamic nuclear polarization in insulating solids. J. Magn. Reson. **253**, 23–35 (2015)
161. Lelli, M., Gajan, D., Lesage, A., Caporini, M.A., Vitzthum, V., Mieville, P., Heroguel, F., Rascon, F., Roussey, A., Thieuleux, C., Boualleg, M., Veyre, L., Bodenhausen, G., Coperet, C., Emsley, L.: Fast characterization of functionalized silica materials by silicon-29 surface-enhanced NMR spectroscopy using dynamic nuclear polarization. J. Am. Chem. Soc. **133**(7), 2104–2107 (2011)
162. Lesage, A., Lelli, M., Gajan, D., Caporini, M.A., Vitzthum, V., Mieville, P., Alauzun, J., Roussey, A., Thieuleux, C., Mehdi, A., Bodenhausen, G., Coperet, C., Emsley, L.: Surface enhanced NMR spectroscopy by dynamic nuclear polarization. J. Am. Chem. Soc. **132**(44), 15459–15461 (2010)
163. Thankamony, A.S.L., Knoche, S., Bothe, S., Drochner, A., Jagtap, A.P., Sigurdsson, S.T., Vogel, H., Etzold, B.J.M., Gutmann, T., Buntkowsky, G.: Characterization of V-Mo-W mixed oxide catalyst surface species by V-51 solid-state dynamic nuclear polarization NMR. J. Phys. Chem. C. **121**(38), 20857–20864 (2017)
164. Lapina, O.B.: Modern ssNMR for heterogeneous catalysis. Catal. Today. **285**, 179–193 (2017)
165. Valla, M., Rossini, A.J., Caillot, M., Chizallet, C., Raybaud, P., Digne, M., Chaumonnot, A., Lesage, A., Emsley, L., van Bokhoven, J.A., Coperet, C.: Atomic description of the Interface between silica and alumina in aluminosilicates through dynamic nuclear polarization surface-enhanced NMR spectroscopy and first-principles calculations. J. Am. Chem. Soc. **137**(33), 10710–10719 (2015)
166. Rossini, A.J., Zagdoun, A., Lelli, M., Lesage, A., Coperet, C., Emsley, L.: Dynamic nuclear polarization surface enhanced NMR spectroscopy. Acc. Chem. Res. **46**(9), 1942–1951 (2013)
167. Lee, D., Duong, N.T., Lafon, O., De Paepe, G.: Primostrato solid-state NMR enhanced by dynamic nuclear polarization: pentacoordinated Al3+ ions are only located at the surface of hydrated gamma-alumina. J. Phys. Chem. C. **118**(43), 25065–25076 (2014)
168. Lund, A., Hsieh, M.F., Siaw, T.A., Han, S.I.: Direct dynamic nuclear polarization targeting catalytically active Al-27 sites. Phys. Chem. Chem. Phys. **17**(38), 25449–25454 (2015)
169. Orlinskii, S.B., Schmidt, J., Baranov, P.G., Donega, C.D., Meijerink, A.: Dynamic nuclear polarization of Zn-67 and H-1 spins by means of shallow donors in ZnO nanoparticles. Phys. Rev. B. **79**(16), 165316 (2009)
170. Wolf, P., Valla, M., Nunez-Zarur, F., Comas-Vives, A., Rossini, A.J., Firth, C., Kallas, H., Lesage, A., Emsley, L., Coperet, C., Hermans, I.: Correlating synthetic methods, morphology, atomic-level structure, and catalytic activity of Sn-beta catalysts. ACS Catal. **6**(7), 4047–4063 (2016)
171. Kobayashi, T., Perras, F.A., Goh, T.W., Metz, T.L., Huang, W.Y., Pruski, M.: DNP-enhanced ultrawideline solid-state NMR spectroscopy: studies of platinum in metal-organic frameworks. J. Phys. Chem. Lett. **7**(13), 2322–2327 (2016)
172. Pump, E., Bendjeriou-Sedjerari, A., Samantaray, M., Abou-Hamad, E., Basset, J.: Dynamic nuclear polarization surface enhanced NMR spectroscopy (DNP-SENS) for highly sensitive surface organometallic chemistry (SOMC). Abstr. Pap. Am. Chem. S. **252** (2016). https://www.morressier.com/o/event/5fc63af903137aa5256c260d/article/5fc63bcb9e0a135cbececed5?contentLibrary=ACS&contentLibraryTitle=American+Chemical+Society&from=%2Flibrary%2FACS%2Fevents%3Fpage%3D2
173. Perras, F.A., Chaudhary, U., Slowing, I.I., Pruski, M.: Probing surface hydrogen bonding and dynamics by natural abundance, multidimensional, O-17 DNP-NMR spectroscopy. J. Phys. Chem. C. **120**(21), 11535–11544 (2016)
174. Blanc, F.: Acidity strength of solid catalysts probed by hyper-polarized natural abundance O-17 NMR spectroscopy. Angew. Chem. Int. Edit. **56**(39), 11694–11696 (2017)
175. Perras, F.A., Wang, Z.R., Naik, P., Slowing, I.I., Pruski, M.: Natural abundance O-17 DNP NMR provides precise O-H distances and insights into the Bronsted acidity of heterogeneous catalysts. Angew. Chem. Int. Edit. **56**(31), 9165–9169 (2017)
176. Camacho-Bunquin, J., Ferrandon, M., Sohn, H., Yang, D.L., Liu, C., Ignacio-de Leon, P.A., Perras, F.A., Pruski, M., Stair, P.C., Delferro, M.: Chemoselective hydrogenation with supported organoplatinum(IV) catalyst on Zn(II)-modified silica. J. Am. Chem. Soc. **140**(11), 3940–3951 (2018)

Nicholas Jaegers received his PhD (chemical engineering) in December of 2019 from Washington State University (WSU), supervised by Dr. Yong Wang. He has worked as a PhD intern at Pacific Northwest National Laboratory (PNNL) for 4 years, focusing on applications of NMR for catalysis under the mentorship of Dr. Jian Zhi Hu, and has published more than 20 peer-reviewed papers.

Nancy M. Washton is a scientist at PNNL with extensive experience in catalyst characterization utilizing NMR. She leads the magnetic resonance capability at the Environmental Molecular Sciences Laboratory user facility and develops in situ technologies relevant to catalysis characterization. Nancy has over 50 publications, 1 patent, and an h-index of 19.

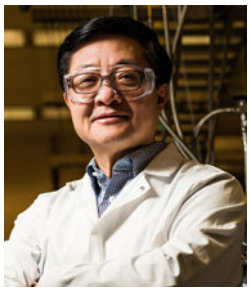

Yong Wang holds joint appointments at PNNL and WSU as the Voiland Distinguished Professor in chemical engineering. Wang has published more than 480 peer-reviewed papers and has been cited more than 23,000 times (h-index: 71). As the inventor of more than 270 issued patents, he has earned 3 R&D 100 awards and is a fellow of AIChE, ACS, RSC, and AAAS.

Jian Zhi Hu is a senior staff scientist of PNNL, principal investigator for multiple NIH and NASA grants, and key investigator of several DOE-BES projects. He has published more than 210 peer-reviewed papers related to NMR with an h-index of 42 and over 6000 Web of Science citations and received 11 US patents and 2 R&D 100 awards.